Title
Transport Properties of Bilayer Graphene Nanoribbons

Permalink
https://escholarship.org/uc/item/72f889js

Author
Wang, Minsheng

Publication Date
2013

Peer reviewed|Thesis/dissertation

UNIVERSITY OF CALIFORNIA

Los Angeles

Transport Properties of Bilayer Graphene nanoribbons

A dissertation submitted in partial satisfaction of the

requirements for the degree Doctor of Philosophy

in Electrical Engineering

by

Minsheng Wang

2013

ABSTRACT OF THE DISSERTATION

Transport Properties of Bilayer Graphene Nanoribbons

by

Minsheng Wang

Doctor of Philosophy in Electrical Engineering

University of California, Los Angeles, 2013

Professor Kang L. Wang, Chair

Motivated by the rising of the carbon electronics and the potential applications of bilayer graphene nanoribbons in both electronics and optics, this thesis focuses on the fundamental transport properties of bilayer graphene nanoribbons. Two types of devices were fabricated from mechanically exfoliated bilayer graphene films, by using nanowires masks and the oxygen plasma etching process. In the back-gated devices, transport gaps and Coulomb blockade effect indicate that the disorder-induced potential landscape creates quantum dots along the nanoribbons and governs the transport property. In the dual-gated devices, the effects of the perpendicular electric field leads to the evolution of the transport gap size and the oscillation strength. The interaction between the potential landscape and the field-induced gap is proposed to explain the observed transport behavior. Our study reveals the dominant factors in the bilayer

graphene nanoribbon transport under different conditions. The physical understanding

presented here points out the possible routes towards future applications.

The dissertation of Minsheng Wang is approved.

Benjamin S. Williams

Robert N. Candler

Hong-Wen Jiang

Kang L. Wang, Committee Chair

University of California, Los Angeles

2013

Table of Content

List of Figures and Tables

Acknowledgements

I would like to thank my PhD Advisor, Professor Kang L. Wang, for giving me the opportunity to study in UCLA, for introducing me into this amazing field, for encouraging me to face difficulties, for challenging me to improve myself, for his guidance and support in the research work and in my life over the years.

I also would like to thank all my colleagues for all the long hours we spent in clean room together, for all the late nights stuck with the measurement setups, for all the sparks from the discussions, and for all the fun we have together in the group events.

Thanks to my parents for respecting my decisions and supporting me unconditionally, always.

Thank you all for making everything I achieved today possible.

Vita

Education

2002-2005   MS in Solid State Electronics, Institute of Microelectronics, Tsinghua University, Beijing, P.R. China.

1998-2002   BS in Electrical Engineering, Tsinghua University, Beijng, P.R. China.

Publications

- Poljak, M.; Song, E. B.; <u>Wang, M.</u>; Suligoj, T.; Wang, K. L., "Influence of Edge Defects, Vacancies, and Potential Fluctuations on Transport Properties of Extremely Scaled Graphene Nanoribbons". *Electron Devices, IEEE Transactions on* **2012,** *PP* (99), 1-8.

- <u>Wang, M.</u>; Song, E. B.; Lee, S.; Tang, J.; Lang, M.; Zeng, C.; Xu, G.; Zhou, Y.; Wang, K. L., "Quantum Dot Behavior in Bilayer Graphene Nanoribbons". *ACS Nano* **2011,** *5* (11), 8769-8773.

- Zhou, Y.; Han, W.; Chang, L.-T.; Xiu, F.; <u>Wang, M.</u>; Oehme, M.; Fischer, I. A.; Schulze, J.; Kawakami, R. K.; Wang, K. L., "Electrical spin injection and transport in germanium". *Phys. Rev. B* **2011,** *84* (12), 125323.

- Song, E. B.; Lian, B.; Kim, S. M.; Lee, S.; Chung, T.-K.; <u>Wang, M.</u>; Zeng, C.; Xu, G.; Wong, K.; Zhou, Y.; Rasool, H. I.; Seo, D. H.; Chung, H.-J.; Heo, J.; Seo, S.; Wang, K. L., "Robust bi-stable memory operation in single-layer graphene ferroelectric memory". *Appl. Phys. Lett.* **2011,** *99* (4), 042109.

- Tang, J.; Wang, C.-Y.; Xiu, F.; Hong, A. J.; Chen, S.; <u>Wang, M.</u>; Zeng, C.; Yang, H.-J.; Tuan, H.-Y.; Tsai, C.-J.; Chen, L. J.; Wang, K. L., "Single-crystalline Ni 2 Ge/Ge/Ni 2 Ge nanowire heterostructure transistors". *Nanotechnology* **2010,** *21* (50), 505704.

- Bai, J.; Cheng, R.; Xiu, F.; Liao, L.; <u>Wang, M.</u>; Shailos, A.; Wang, K. L.; Huang, Y.; Duan, X., "Very Large Magnetoresistance in Graphene Nanoribbons". *Nat Nano* **2010,** *5* (9), 655-659.

- Xu, G.; Torres, C. M.; Zhang, Y.; Liu, F.; Song, E. B.; <u>Wang, M.</u>; Zhou, Y.; Zeng, C.; Wang, K. L., "Effect of Spatial Charge Inhomogeneity on 1/f Noise Behavior in Graphene". *Nano Lett.* **2010,** *10* (9), 3312-3317.

- Zeng, C.; <u>Wang, M.</u>; Zhou, Y.; Lang, M.; Lian, B.; Song, E.; Xu, G.; Tang, J.; Torres, C.; Wang, K. L., "Tunneling spectroscopy of metal-oxide-graphene structure". *Appl. Phys. Lett.* **2010,** *97* (3), 032104.

x

- Song, E. B.; Lian, B.; Xu, G.; Yuan, B.; Zeng, C.; Chen, A.; <u>Wang, M.</u>; Kim, S.; Lang, M.; Zhou, Y.; Wang, K. L., "Visibility and Raman spectroscopy of mono and bilayer graphene on crystalline silicon". *Appl. Phys. Lett.* **2010,** *96* (8), 081911.

- Kalantar-zadeh, K.; Tang, J.; <u>Wang, M.</u>; Wang, K. L.; Shailos, A.; Galatsis, K.; Kojima, R.; Strong, V.; Lech, A.; Wlodarski, W.; Kaner, R. B., "Synthesis of nanometre-thick MoO3 sheets". *Nanoscale* **2009,** *2* (3), 429-433

- Allen, M. J.; <u>Wang, M.</u>; Jannuzzi, S. A. V.; Yang, Y.; Wang, K. L.; Kaner, R. B., "Chemically induced folding of single and bilayer graphene". *Chemical Communications* **2009,** (41), 6285-6287.

- Gilje, S.; Han, S.; <u>Wang, M.</u>; Wang, K. L.; Kaner, R. B., "A Chemical Route to Graphene for Device Applications". *Nano Lett.* **2007,** *7* (11), 3394-3398.

- Han, S.; <u>Wang, M.</u>; Gilje, S.; Kaner, R. B.; Wang, K. L. "Semiconducting graphite oxide films for large scale carbon based electronics". *Nanotechnology, 2007. IEEE-NANO 2007. 7th IEEE Conference on*, 2-5 Aug. 2007; 2007; pp 1170-1173.

Chapter 1

Introduction

For over half a century, semiconductor electronic devices have been the driving force of the world economy, with the capability of scaling down according to Moore's Law.[1] At the same time, people are constantly looking for new materials, new device structures and new logics to prepare for the end of this scaling down path. Among the promising candidates, graphene based electronic materials have attracted many research efforts, owing to their extraordinary properties and potential applications in many fields, represented by the most intensively studied members: single-layer graphene (SLG), bilayer graphene (BLG) and single-layer graphene nanoribbon (SL-GNR).[2-4] As the most closely related member in the family, the study on bilayer graphene nanoribbon (BL-GNR) has been limited until recently, when interesting potential applications have been predicted by theoretical calculations.[5-10] To obtain fundamental knowledge and facilitate future developments of BL-GNRs, this thesis is focused on the transport properties of BL-GNRs. For a better understanding, the background knowledge on the electronic properties of SLG, BLG, and SL-GNR will be reviewed.

1.1 Background

1.1.1 Electronic properties of single-layer graphene (SLG)

As a single layer of carbon atoms with a honey comb lattice, singe-layer graphene is considered the building block of carbon electronics. Various carbon materials in different dimensions (e.g. graphite, carbon nanotube and fullerene) can all be constructed from these single layer sheets (Figure 1.1).
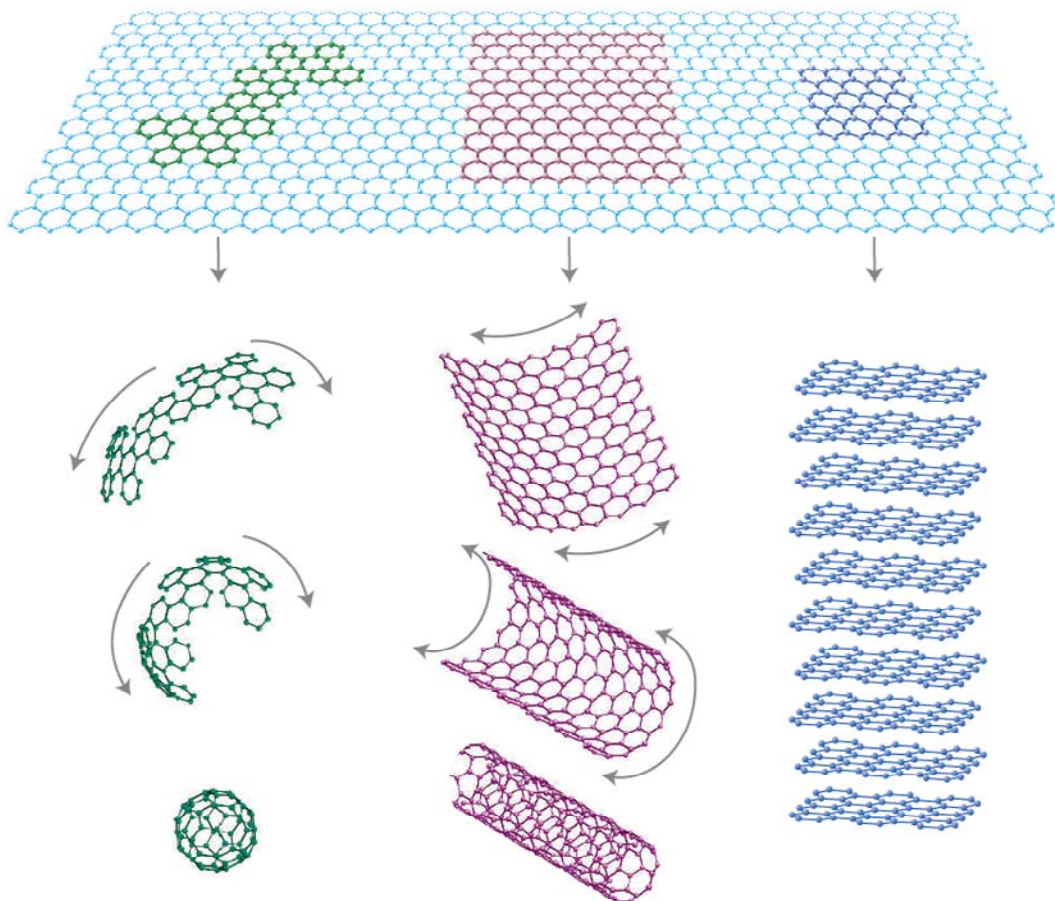
Figure 1.1 Carbon electronic materials in different dimensions. 3D Graphite (Right), 1D carbon nanotube (Middle) and 0D Fullerene (Left) can all be constructed from a 2D graphene sheet (Top). [From A. K. Geim et al., Nat. Mater, 6(3), 183-191, 2007].[2]

Unlike other carbon allotropes, the physical existence of such a pure 2D lattice was not proven until 2005, when quantum Hall features specially belonging to SLG were observed in experiments.[11, 12] On the contrary to the late experimental discovery, the theoretical interests on graphene can be traced back to late 1940s, when the special features in the graphene band structure were calculated for the first time.[13]
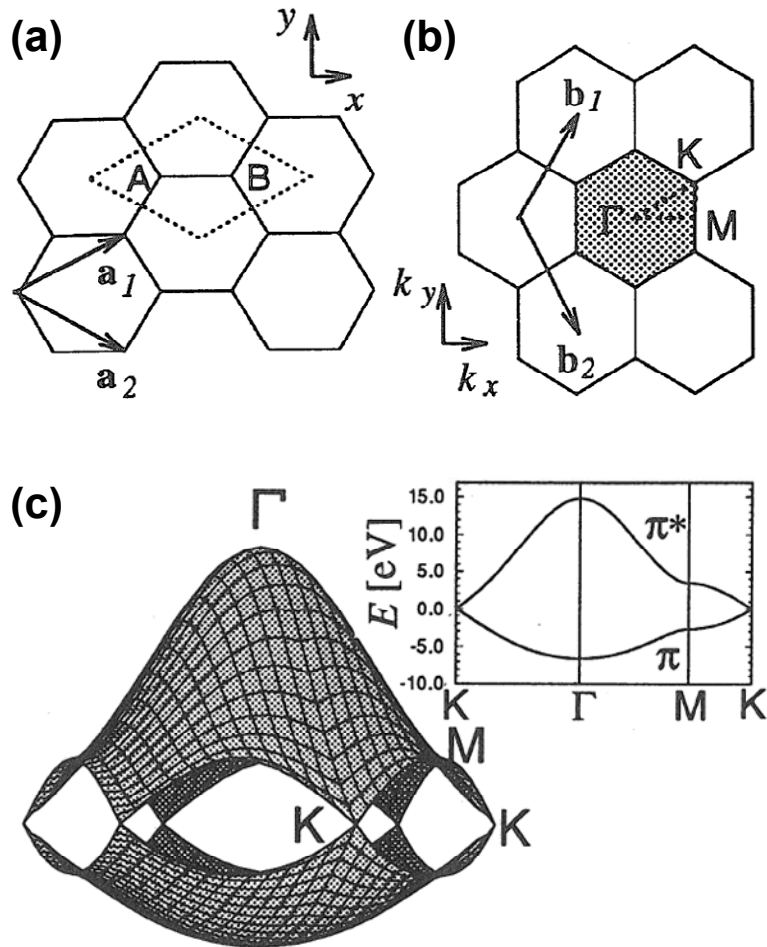
Figure 1.2 Graphene lattice and tight binding band diagram. (a) Real space lattice and unit cell (dotted rhombus). (b) Reciprocal lattice and Brillouin zone (shaded hexagon). (c) two-band tight binding band diagram of graphene. Inset: energy

dispersion along high symmetry lines. [From R. Saito et al., World Scientific: 35, 1998].[14]

Despite the rich physics introduced by graphene, its band structure is readily described by a simple two-band tight binding model. Considering only the P_z orbital (π electron) out of four valence electrons and the nearest-neighbor hopping energy, the tight binding Hamiltonian of graphene can be written as:

$$H = \begin{bmatrix} 0 & tf(k) \\ tf(k)^* & 0 \end{bmatrix}; f(k) = e^{i\vec{k}\cdot\vec{R_1}} + e^{i\vec{k}\cdot\vec{R_2}} + e^{i\vec{k}\cdot\vec{R_3}}$$ Eq.(1-1)

Where t (~ 2.7eV) is the nearest-neighbor hopping energy and $\mathbf{R_i}$ (i= 1,2,3) is the location vector of the nearest-neighbor atoms.[14] The calculated band structure is shown in Figure 1.2c. It is clear from the diagram that there is no band gap in SLG. Instead, the conduction band and the valence band meet at the **K** points of the first Brillouin zone, which is also referred to as the Dirac point in graphene related literature. Near this point, the dispersion can be simply represented by the following linear equation:

$$E = v_F \hbar k$$ Eq.(1-2)

Where v_F is the Fermi velocity (~10^6 m/s), $\hbar$ is the Plank constant and k is the electron momentum relative to the Dirac point.

This very unique linear dispersion leads to the zero effective mass, the vanishing density of states near the Dirac point and the suppression of the backscattering (Klein tunneling).[15, 16] Reflected in the graphene field effect transistors (GFET), high intrinsic

carrier mobility, ambipolar behavior and efficient field modulation are achieved by many research groups.[17-19] Despite the lack of the off state from the semi-metallic nature, GFET is still considered as a promising candidate for high speed electronics applications, such as RF transistors[20-22] and frequency doublers.[23, 24] At the same time, much effort has been made and current research is still ongoing to explore new device structures from different aspects, such as PN junctions,[25-27] field effect tunneling transistors,[28, 29] super-lattices,[4, 30] spin FETs[31-34] and hot electron transistors,[35-37] in the attempt to utilize the special properties of SLG to achieve new generation of electronic devices.

1.1.2 Electronic properties of bilayer graphene (BLG)

The concept of bilayer graphene is entirely different from simply putting one layer of carbon atoms on top of another. The key features to understand the remarkable differences between bilayer and single-layer graphene are the relative position (stacking order) and the electron hoping energy between atoms in different layers. Among the naturally formed bilayer graphene samples, the mostly found order is A-B stacking (also called Bernal stacking).[38, 39] As illustrated in Figure 1.3a, the sub-lattice A2 sits right on top of sub-lattice B1, while B2 projects itself at the center of the equilateral triangle formed by A1 atoms. Since bilayer graphene has the same lattice type in both real and reciprocal space as single-layer graphene (Figure1.3b), its primitive cell can be constructed by the primitive cells from the two layers. Thus, the Hamiltonian around the Dirac point can be written from the eigenstates of single-layer graphene:

5

$$H_K = \begin{bmatrix} -\Delta & v_F k & 0 & 3\gamma_3 a k^* \\ v_F k & -\Delta & \gamma_1 & 0 \\ 0 & \gamma_1 & \Delta & v_F k \\ 3\gamma_3 a k & 0 & v_F k & \Delta \end{bmatrix}$$

Eq.(1-3)

Where v_F is the Fermi velocity in single layer graphene, γ1 (~ 300 meV)[40, 41] is the hopping integral between B1 and A2, γ3 is the hopping integral between A1 and B2, a is the lattice constant, k is the electron momentum relative to the Dirac point and the value 2Δ is the potential difference between the two carbon layers. It is easy to see that the top-left and bottom-right 2×2 matrices represent the Hamiltonian of the single layers. And the off-diagonal matrix elements come from the coupling between layers.
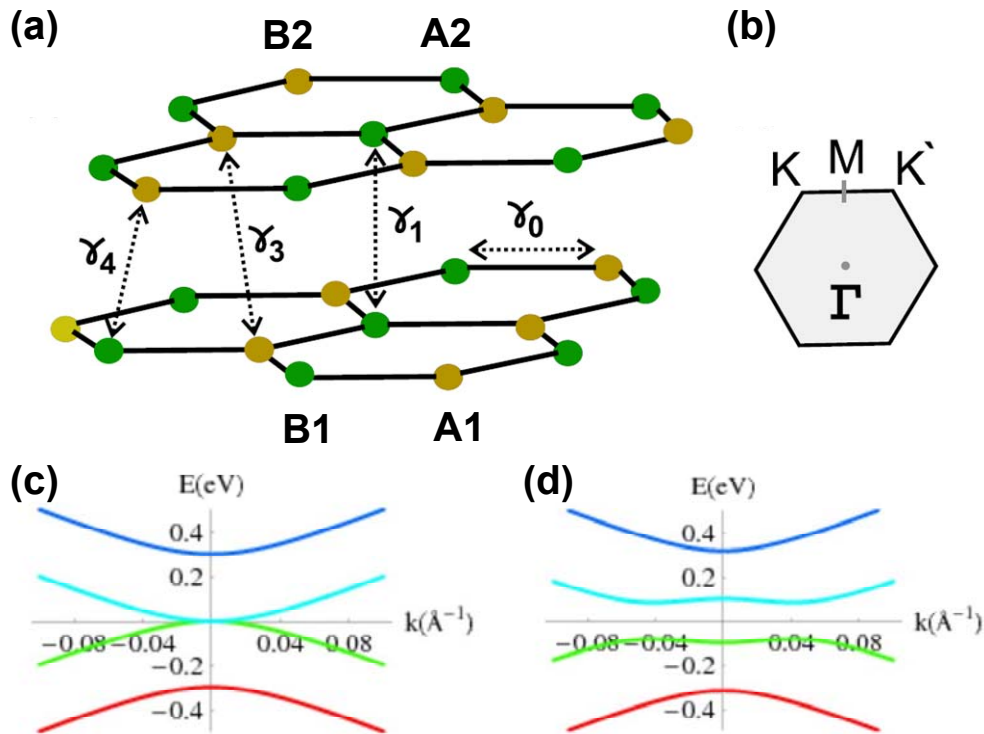
Figure 1.3 Lattice structure and band diagram of bilayer graphene. (a) Bilayer graphene lattice: A1 (green) and B1 (brown) represent the sublattice from the bottom layer, while A2 (brown) and B2 (green) mark the sublattice from top layer. γ0 is the in-

plane coupling energy between A1B1, γ1 is the interlayer coupling between B1A2. The coupling strength between A1B2 (γ3) and B1B2 (γ4) are ignored in the first order tight binding calculations. (b) The first Brillion zone of bilayer graphene. (c) Bilayer graphene band diagram when Δ = 0. (d) Bilayer graphene band diagram when Δ ≠ 0. [From A. H. C. Neto et al., Rev. Mod. Phys. 81(1), 183-54, 2009].[40]

In the simplest case, when the two layers are at the same potential (Δ = 0), the solution of the above Hamiltonian gives the band diagram in Figure 1.3c. The four-band splitting is expected in bilayer graphene from the tight binding point of view.[42] The splitting energy is exactly γ1 (~ 300 meV), which is relatively large given the separations from both the conduction band and the valence band. So in most of the electrical measurements discussed in this study, the higher energy subbands make no contributions. For the low energy subbands, the dispersion can be directly obtained from the Hamiltonian:

$$E_{k,\pm} \approx \pm \frac{v_F^2 k^2}{\gamma_1}$$
<div align="right">Eq.(1-4)</div>

The similarities to single-layer graphene are the zero-gap feature and the existence of the Dirac point. However the linear dispersion curves are changed back to a parabolic shape. This change has profound effects on the electronic properties of bilayer graphene and its transport behaviors. The effective mass becomes finite and the density of state near the band edge (Dirac point) takes a constant value in bilayer graphene. This explains why in back-gated bilayer GFETs, higher minimum

conductance and less effective gate modulation are usually observed, compared to single-layer GFETs.[19]

The equation of the band diagram becomes more complicated once a potential difference is present between the layers. Under this situation, the expressions for the low energy subbands become:

$$E_{k,\pm} \approx \pm\left(\Delta - \frac{2\Delta v_F^2 k^2}{\gamma_1} + \frac{v_F^4 k^4}{2\gamma_1^2\Delta}\right) \qquad\qquad Eq.(1\text{-}5)$$

As shown in Figure 1.3d, a band gap is formed around the Dirac point. To the first order, the size of this band gap is approximately 2Δ, which is exactly the potential difference between layers.[41, 43] This gap is also referred to as the field-induced gap (ΔE$_{FD}$) in bilayer graphene related literature, since the potential difference between two planes with fixed distance is equivalent to a perpendicular electric field. The potential difference can be created by putting different charge carriers in the two layers. Both chemical doping[44] and electrical doping (gate modulation)[45-51] have been successfully achieved in A-B stacking bilayer graphene. However, the direct and relatively accurate observations of ΔE$_{FD}$ were mostly made by optical methods. In electrical measurements, even though a high on/off ratio of 100 at room temperature can be achieved, the accuracy of the ΔE$_{FD}$ estimation suffers from the existence of the disorders in the system.

1.1.3 Electronics properties of single-layer graphene nanoribbons (SL-GNR)

As mentioned in 1.1.1, GFETs suffer from the high leakage current at the off state, thus are not suitable for logic applications. To increase on/off ratio, graphene nanoribbons (SL-GNRs) were studied soon after the rising of graphene.[52, 53] The idea is to use quantum confinement to create an energy gap in this otherwise gapless material, which is supported by several theoretical predictions that remarkable energy gaps can exist in narrow SL-GNRs with certain ideal edge configurations.[54-57] Indeed, scalable gap-like behaviors were observed in electrical measurements.[53] However, later on, together with the detailed characterization of the graphene surface potential[58] and the nanoribbon edges[59-61], researchers realized the insulating state is not from a real quantum confinement gap but a so-called transport gap (ΔE_{TR}), representing the blockade effect in the carrier transport process. Two models have been developed for the formation of ΔE_{TR} in SL-GNRs: the spontaneously formed quantum dots[62] and the Anderson localization from the defects/edges states.[63, 64] Although the existence of both phenomena is generally accepted, it is still debated between research groups that which one has the dominant effect, especially because of the large differences between the SL-GNRs obtained by different groups.[65-73] Nevertheless, high on/off ratios (up to 10^6) are achieved in some extremely scaled SL-GNRs.[74] At this scale, however, SL-GNRs are getting more sensitive to the environment (e.g. charge impurities) and the extra scattering from edges. As a result, carrier mobility reduces dramatically in SL-GNRs compared to graphene and CNT.[74, 75]

Beside transistors, other applications, such as field controlled ferromagnetisms,[76] are predicted for SL-GNRs as well. However, a perfect edge is also required for such devices to work properly.

1.2 Motivation and task of the work

Compared to its counterpart SL-GNR, the study of BL-GNR was quite limited. Similarities are anticipated considering some of the common properties of single-layer and bilayer graphene, such as semi-metallic band structure and sensitivity to the disorders, while interesting new phenomena are expected when the interlayer coupling is involved.[40]

On the theoretical front, band gap opening is also possible but relying on the edge types as in SL-GNRs.[77, 78] At the same time, BL-GNRs have been predicted to exhibit strong optical responses in the terazhertz regime,[5, 6] and tunable magnetic properties[7-10] for photonics and spintronics applications.

On the experimental side, to our best knowledge, little has been done on BL-GNRs, except some room temperature characterization[79] and noise measurements from the variability point of view.[80, 81] The fundamental transport properties of BL-GNRs and especially the effects from the field-induced gap had not been explored until the study presented in this thesis.

In the following chapters, special fabrication issues will be introduced in Chapter 2 and the transport properties of two types of devices, back-gated BL-GNRs and dual-gated BL-GNRs will be discussed in Chapter 3 and Chapter 4 respectively.

Chapter 2

Fabrication and measurement of bilayer graphene nanoribbon devices

In this chapter, the fabrication process for bilayer graphene nanoribbon (BL-GNR) devices will be described in detail. Owing to the novelty of graphene and related materials (including BL-GNR), the fabrication methods are relatively immature. Furthermore, because of the nature of some steps (e.g., the mechanical exfoliation process), the yield is not very high and many practices and repeats are required to gain satisfactory results. Nevertheless, these methods are still chosen over their alternatives to avoid possible complications in the analysis, since the purpose is to understand the physics instead of mass production at the current stage. The measurement setups are also described at the end of the chapter.

Based on the methods for SL-GNR fabrication, there are three possible ways to obtain BL-GNRs: etching graphene films, [53, 69-71, 82] unzipping carbon nanotubes (CNTs)[83] and deriving nanoribbons chemically.[84] Each method has its own merits and disadvantages. For unzipping carbon nanotubes, the starting material has to be double wall carbon nanotubes. Also the width of the top layer will be different from the width of the bottom layer, owing to the original diameter difference. This may be desirable for special applications,[8] but not for general purposes. For deriving nanoribbons chemically, devices with different layer numbers are produced at the same time. The percentage of each type is determined by process parameters. Hence, a secondary method is required to select the bilayer ribbons (e.g. Raman or AFM), whose accuracy suffers

from the small device size or the surface interaction. So in the context of fabricating BL-GNRs, the most reliable way is to start from bilayer graphene films, whose layer number and stacking order can be clearly determined at large scale, and then pattern down to nanoribbons.

2.1 Obtain single to few layer graphene films

2.1.1 Mechanical exfoliation

The starting graphene films in this work are produced by the mechanical exfoliation method, also known as the scotch tape method, which has been used to make high quality single to few layer graphene films since 2004.[85]

This method starts with placing a small piece of graphite, such as Kish graphite, natural graphite or highly oriented pyrolytic graphite (HOPG), usually several millimeters in diameter and less than one millimeter in thickness, onto a stripe of scotch tape. Then we fold and unfold the tape repeatedly. Due to the layered structure of graphite and the weak interaction between layers,[86] thin flakes of graphite will be separated and spread on the tape surface. An example of the scotch tape surface after the folding process is shown in Figure 2.1b. Then the tape will be pressed facedown to a clean substrate piece (usually degenerately doped silicon with 300 nm thermally grown oxide). After pushing the back side of the tape against the substrate gently, the tape will be removed from the substrate surface in a slow and controlled motion. The key concept of the mechanical exfoliation process is to utilize the Van der Waals force between the freshly cleaved graphite surface and the relatively clean flat substrate surface to hold down the

graphene (see Figure 2.1a). Here the clean graphite surface is created by the repeated folding and the target substrate must be treated with proper cleaning processes.

(a)

(b)

(c)

10 µm
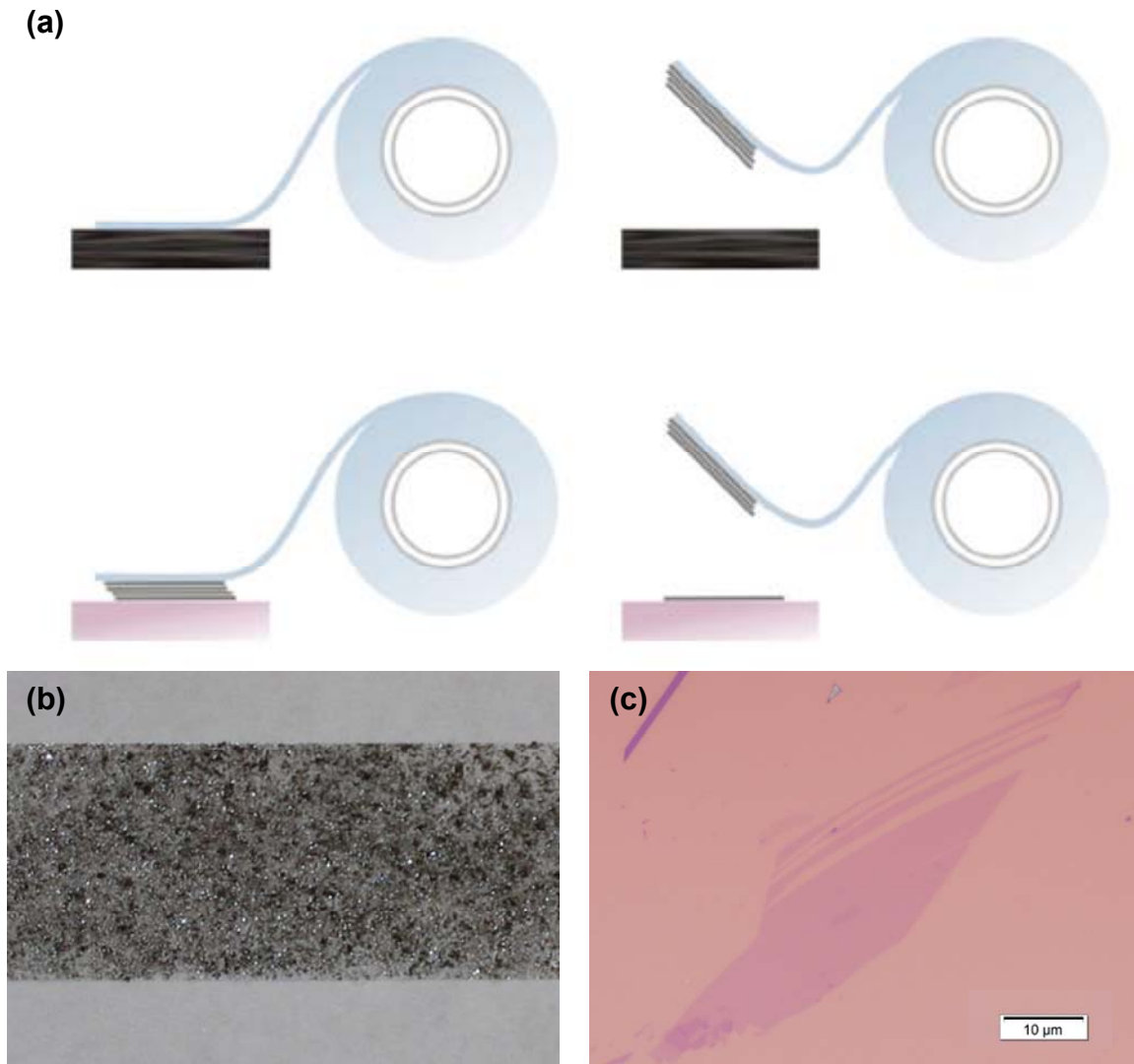
Figure 2.1 Mechanical exfoliation process. (a) Schematic of the mechanical exfoliation process. [From K. S. Novoselov et al., Rev. Mod. Phys. 83(3), 836-849, 2011].[4] (b) Typical tape surface after exfoliating graphite. (c) An exfoliated bilayer graphene film on a typical SiO_2 (300nm)/Si substrate. The scale bar equals to 10 micrometers.

As we can see from the above description, this method is not very efficient. Many steps cannot be well controlled. Instead, they largely rely on experience and practice. Nevertheless, even though the efficiency and the repeatability of this method are not able to match up to industrial standards, the quality and the size of the produced films are well fitted to the needs of scientific research.

Beside the low efficiency and repeatability issues, there are several important details in the process, which can affect the results greatly.

One of the major problems in the mechanical exfoliation process is the randomness of the size, shape and position of the produced films. To be able to locate the desired films and facilitate the following fabrication steps, the substrates are usually pre-patterned with markers, numbers and large size pads. These patterns are fabricated by traditional photolithography and lift-off process, which easily leaves photo resist residue on the substrate. This can reduce the adhesion between graphene and the substrate. So an oxygen plasma cleaning process is a very important yet easily ignored step. The quantity and quality of the produced graphene films will be severely degraded if this cleaning step is skipped.

The height of the pre-patterned marks, numbers and pads can also be a potential issue to the yield, since it may prevent the close contact between the tape and the substrate. One solution is to leave enough space between these pre-patterned features. As long as the spacing is much larger than the possible size of the graphene films, it will not affect the results very much.

An alternative method is to do the mechanical exfoliation first on clean out-of-box substrates without going through the photolithography step. However, once the films are deposited on the substrate, patterning of the markers and numbers is still needed for the following device fabrication. Although the adhesion and the interface between graphene and the substrate will not be affected, photo-resist residue will be induced on top of the existing graphene films.[87] This residue can't be removed by oxygen plasma owing to the nature of carbon materials. It has certain chance to degrade the contact between graphene and source-drain metals in the later process steps. There are also chances that the later patterned marks, numbers and pads may land on top of the exfoliated graphene films, further reducing the already low yield of the whole process.

Another consideration is the choice of the tape. Different researchers tend to use different kinds of tapes. The purpose is to get a high yield of graphene films, without leaving too much tap residue on the substrate. On the folded tape, there are patches not covered by graphite flakers but exposed bare tape surface. When pushed down, the adhesive materials on the tape will be transferred to the substrate at the same time. This residue sometime can be very close to the graphene film, and may move around during the following fabrication steps causing contamination on graphene. Because graphene itself is fragile to oxidizers, the choice of chemicals the can be used to remove residues is limited. The chemicals we have tried in our study including acetone, isopropyl alcohol (IPA), PG remover and N-Methyl-2-pyrrolidone (NMP). It has been proved that completely removal of this residue without damaging graphene is very hard. The choice of good tapes can in a sense alleviate the severeness of this problem. The '3M Magic Tape' is a good candidate based on our experiences.

2.1.2 Grown and transferred from Ni and Cu

One of the alternative ways of getting thin graphene films is to use chemical vapor deposition (CVD) to synthesize them on a transition metal surface, such as Cu, Ni. Then, the films can be transferred onto almost any target substrates. Both the growth and the transfer process have been intensively studied by several research groups[88-90] to obtain large size uniform graphene films at low cost for production and application purpose. In fact, large size flexible displays using single-layer CVD graphene as transparent and flexible electrodes have been demonstrated by Samsung in 2010.[91]

However, for this particular project, the CVD grown graphene films are not good candidates as the starting material for two reasons. First, most of the growth effort has been put in the development of single-layer graphene films, which are very successfully achieved on copper substrates. However, the growth of bilayer graphene films with A-B stacking order was not well developed until recently.[92] Second, the nature of the CVD growth of graphene decides that the crystallinity of the grown film is not in long range order. Domains with different orientations will form in one continuous film depending on the crystallinity of the metal substrate.[93] Owing to the nature of the patterning methods we can use to obtain graphene nanoribbons at this stage, there is no guarantee that the produced ribbons will be formed on a single domain. If there are domain boundaries within a nanoribbon, further complications will be introduced into the already complicated system. Hence, even if the CVD grown A-B stacking bilayer graphene is available, it will not be the preferred choice for this project.

It may be interesting to study the effect of domain boundaries on the transport properties of single-layer or bilayer graphene nanoribbons in the future, using CVD

graphene as the starting material. In that case, surface scanning methods with atomic resolution are needed to identify the grain boundaries in the nanoribbons.

2.1.3 CVD growth from silicon carbide substrates

Another way of growing thin graphene films is the high temperature growth on silicon carbide (SiC) substrates. The idea is based on the fact that along certain crystal orientation the SiC substrates have alternating silicon face and carbon face, with similar crystal structure compared to graphene. This enables the layer by layer epitaxial growth of the carbon atoms under controlled conditions.[94]

The drawbacks of this method include the high cost of the SiC substrate, the requirements of high temperature and high level vacuum. And for the growth of bilayer graphene, even though SiC is a insulator, the wetting layer presented in the epitaxial growth is still troublesome for the electronic characterization. Also the dual-gated structure is hard to be fabricated on SiC substrates. Furthermore, the existence of grain boundaries is still a potential problem. For all the above reasons, graphene films grown on SiC substrates are also not suitable for this project.

2.2 Identify bilayer graphene films

After we obtained the graphene films by exfoliation on SiO_2/Si substrates, the substrates are then subjected to inspection under regular microscopes. Even with atomic layer thickness, single to few layer graphene films can still be located by eyes given the right thickness of the underneath layers, i.e., 300 nm thermal SiO_2 on Si.[85] The

next thing is to identify the layer number and stacking order of these graphene films and select the A-B stacking bilayer ones.

2.2.1 Optical contrast under microscope

Even with only one atomic layer, graphene has certain light absorption and reflection. This gives the different contrast for the graphene films with different layer numbers. Experiences can be gained by enough practices to roughly tell single-layer and bilayer graphene films just through the microscopes. At the same time, computer based digital image processing can certainly be used to distinguish graphene films with different layer numbers, i.e., in the pictures taken by a microscope, the brightness of the layer can be one of the evidence of single or bilayer graphene films. However, the thickness of the silicon oxide on silicon substrates can vary from wafer to wafer and sample to sample. This brings difficulties to the inspection by bare eyes. In this case, calibrations need to be done at the beginning by incorporating other methods. Furthermore, from the microscope pictures, the stacking order cannot be identified for a bilayer graphene film. Despite the different electronic properties of bilayer graphene with different stacking orders,[38, 95] there is no reported difference on their optical contrast.

It is also worth noting that if other substrates need to be used for different applications, a substrate material stack needs to be developed based on the multiple-layer-reflection model under lights with different wavelengths.[96] This has been developed in other work within our group. For an example, we have successfully

developed right substrate stacks that enable us to find single-layer and bilayer graphene films in close contact to silicon and lead-zirconate-titanate (PZT) substrates.[97, 98]

2.2.2 Atomic Force Microscopy (AFM)

Another way of identifying the layer number of a graphene film is to directly measure the thickness by atomic force microscopy (AFM). AFM is a widely used method to characterize surface morphology with atomic resolution. In this case, the step height on the edges of graphene films can be characterized and may be used to obtain the layer number.

Based on the information extracted from graphite, the thickness of a single carbon atom layer is ~4 angstrom. However, owing to the unavoidable surface absorptions (e.g., water molecules from the atmosphere and the possible fabrication residue), the measured thickness for single-layer graphene films vary from 0.4 nm to 1.2 nm on the most commonly used SiO_2/Si substrates. On the other hand, the 4 angstroms step height between graphene films with one layer number difference can be accurately detected (see Figure 2.2). As a result, the thickness measured by AFM can range from 0.8 nm to 1.6 nm for a bilayer graphene film, and from 1.2 nm to 2.0 nm for a tri-layer graphene film. Therefore, it is not possible to distinguish the bilayer graphene ones from single-layer and tri-layer graphene films solely based on the AFM measurement results.
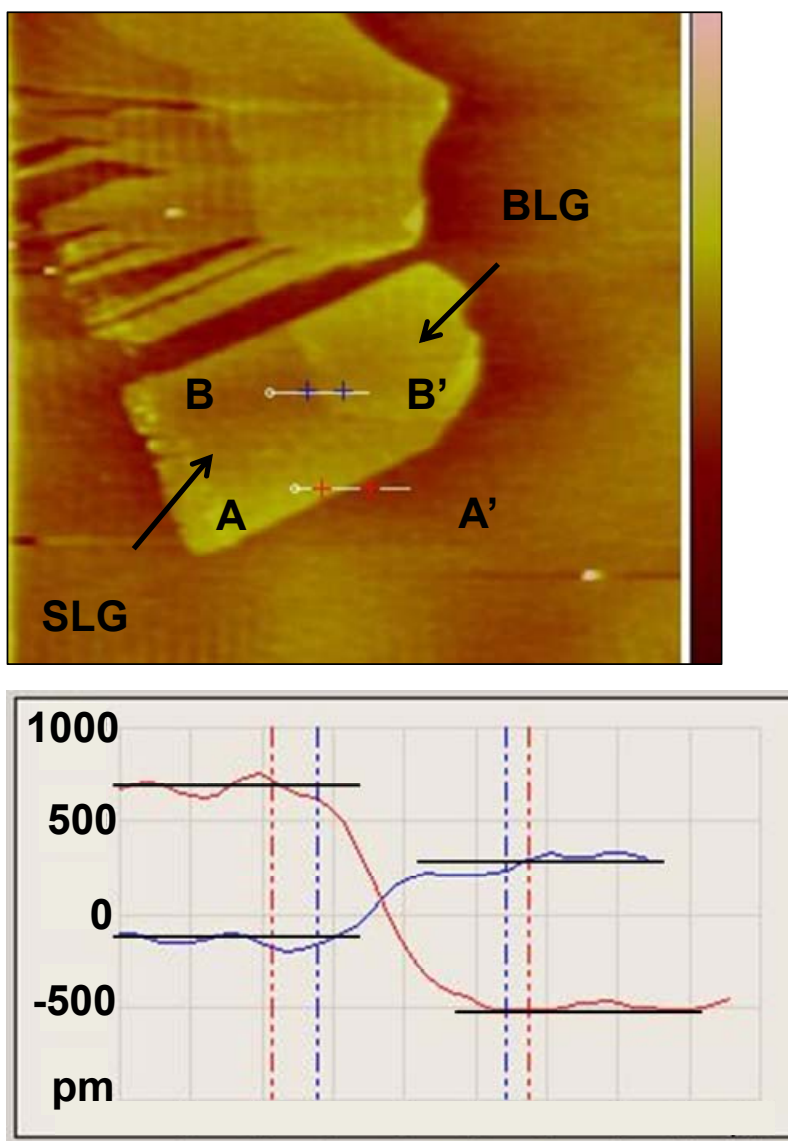
Figure 2.2 AFM measurements on single and bilayer graphene films. AA' (line with red markers) measures the step height between a single-layer graphene film and the substrate (~1.2 nm); BB' (line with blue markers) measures the step between the single-layer graphene film and an adjacent bilayer graphene film (~0.4 nm). The layer numbers are confirmed by micro-Raman spectra.

From the above discussion, AFM itself is not a good technique to determine the layer number of a graphene film. Some other calibration methods must be used to reduce the possible variations. Furthermore, AFM is a contacting method, which may introduce potential contamination to graphene or damage the lattice, if wrong parameters are used. For this consideration, tapping mode is preferred over contacting mode, if AFM is absolutely needed for graphene samples (e.g., to measure the width of a graphene nanoribbon).

2.2.3 Raman spectroscopy

Raman spectroscopy is a fast, easy, non-destructive and very accurate way to identify single-layer and bilayer graphene. There are three major signals used in the Raman characterization of a graphene film, D band, G band and 2D band. The D band signal (~ 1345 cm^{-1}) represents defects in the graphene/graphite system. It cannot be ignored in graphite samples because of the flicker boundaries inside, but becomes almost invisible in the mechanical exfoliated graphene films except near the edges.[99] The G band signal usually shows a sharp single peak near ~ 1580 cm^{-1}. It corresponds to the E_{2g} phonon from the in-plane oscillation of the graphene lattice.[100] So the intensity of the G band signal increases proportionally with the layer number in graphene thin films. This can be one of the signatures to distinguish single-layer, bilayer and tri-layer graphene. The 2D band signal is from the double resonance Raman process, which involves both electron and phonon bands, as shown in Figure 2.3. An electron can be excited by an incident photon. Then it interacts with two phonons and then goes back its original state by emitting another photon with a different energy.

Because of the difference in the band structure, there is only one process contributing strongly to the single-layer graphene spectrum (Figure 2.3a), while four choices exist in the bilayer graphene case (Figure 2.3b).
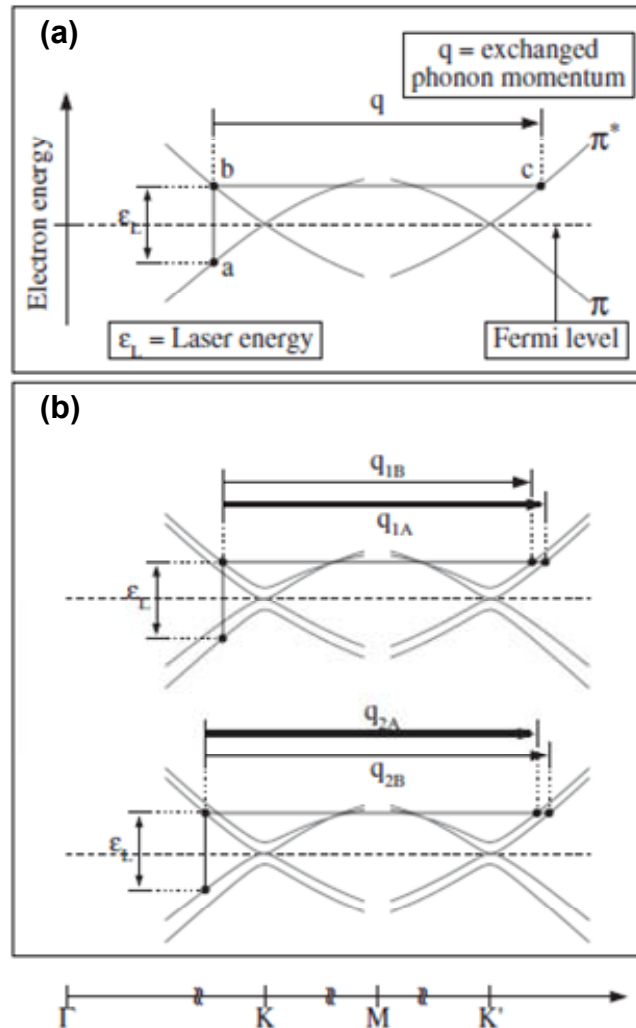
Figure 2.3 Double resonant Raman process in (a) single-layer and (b) bilayer graphene. Only the $q > K$ phonons are illustrated. The other two types ($q \sim K$ and $q < K$) have much smaller contribution to the Raman intensity. [From A. C. Ferrari et al., Phys. Rev. Lett. 97(18), 187401-4, 2006][101]

As a result, the single-layer 2D band shows a sharp single Lorentzian peak at ~2700 cm^{-1} (Figure 2.4 top spectrum), while the bilayer 2D band can always be decomposed to four peaks near the same wave number (Figure 2.4 middle spectrum). Although the exact positions of the G band and 2D band peaks are related to the doping of the graphene films through the electron-phonon coupling effect,[99] the peak spacings between these four peaks are always very consistent through our experiments (~ 35, 20 and 15 cm^{-1}) and in good agreement with the theoretical prediction.[101] For thicker films (e.g., trilayer graphene), the 2D band splitting can be much more complicated, so that simple fitting cannot be obtained (Figure 2.4 bottom spectrum).[102] Therefore, the Raman spectrum provides us a very accurate and efficient way to select AB stacking bilayer ones from all the exfoliated graphene films.
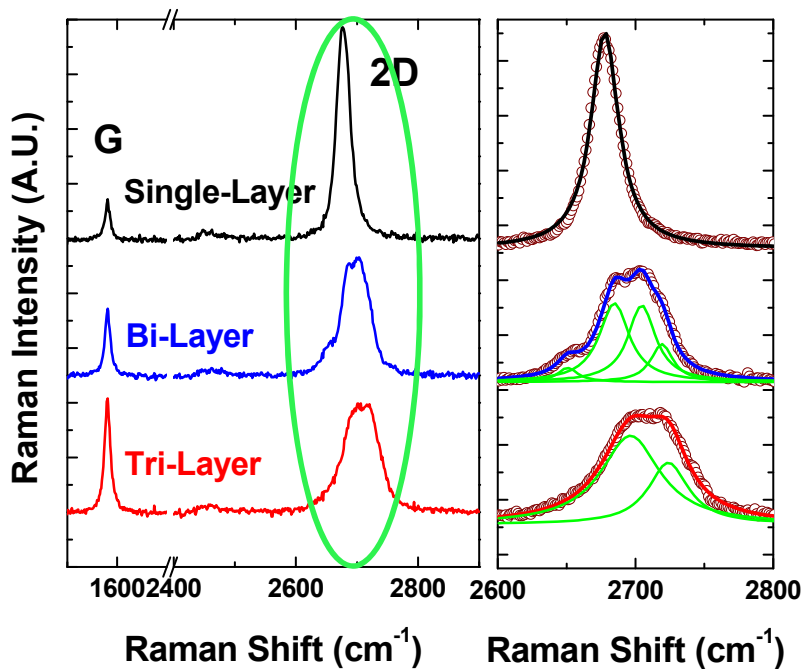
Figure 2.4 Comparison of Raman spectra for single-layer, bilayer and tri-layer graphene. The G band signal intensity increase with layer numbers. The 2D band

signal: a single sharp peak in single-layer graphene (top), a typical four-peak decomposition in bilayer graphene (middle) and two-peak splitting in Trilayer graphene (bottom). The layer number of the trilayer graphene is confirmed by the AFM measured step height from an adjacent bilayer piece. The incident laser wavelength: 514 nm.

2.2.4 Quantum Hall effect (QHE)

The signature of the bilayer graphene band structure can also be found in the quantum Hall measurements, which distinguishes itself from both regular two dimensional semiconductors and single-layer graphene films (Figure 2.5).
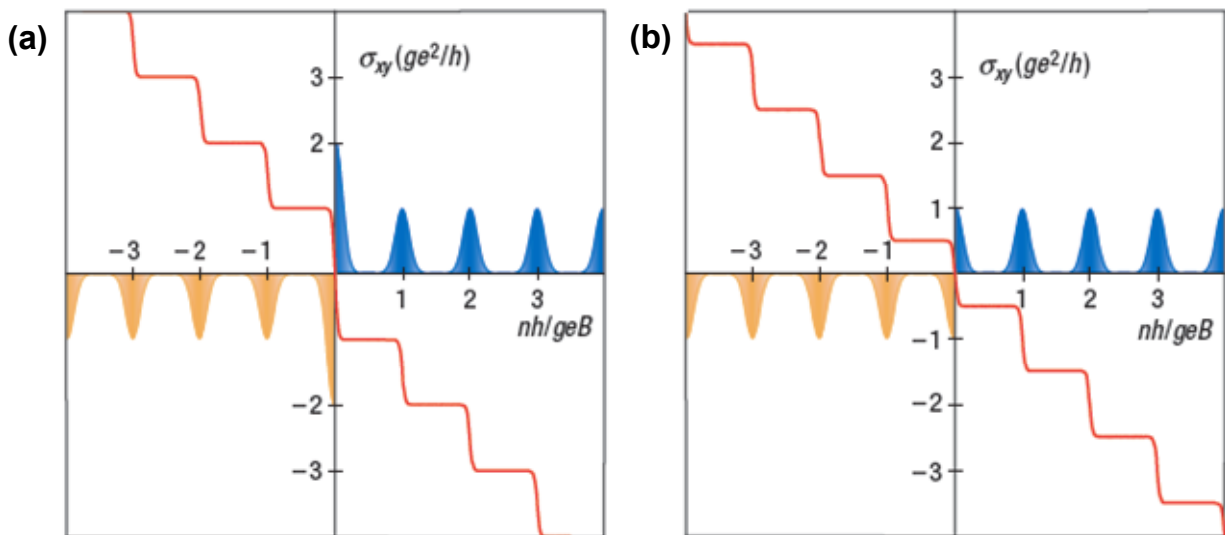
Figure 2.5 Quantum Hall effect in (a) single-layer graphene and (b) bilayer graphene. The conductivity step at the Dirac point (n ~ 0) is $2ge^2/h$ in bilayer graphene compared to ge^2/h in single-layer graphene, indicating a double degenerated lowest Landau level. This step is completely missing in the quantum Hall effect from regular 2D

semiconductors, owing to the missing 0th order Landau level. [From K. S. Novoselov et al., Nat. Phys. 2(3), 177-180, 2006].[103]

The disadvantages of this method are also obvious. The whole fabrication process including etching of the Hall bar structure and putting on at least five contacts needs to be done before the measurements, not to mention the high magnetic field and the low temperature requirements. So this method is usually used to fabricate control devices to examine the quality of graphene films, rather than select bilayer graphene pieces at the beginning stage of the whole process.

2.3 Patterning BL-GNR devices

After selecting the AB stacking bilayer graphene films, the next step is to etch them into nanoribbons. This requires masks with a proper size and an etching process to transfer the shape of the mask to the bilayer graphene film. The masks can be made from either the electron beam lithography (EBL), chemical synthesis methods[104] or transferred nanowires,[82] while the etching can be done by either ion milling with bombardment by non-reactive atoms (argon plasma) or chemical reactions with bias radicals (oxygen plasma).

For the masks from EBL and the chemical synthesis methods, the etching processes produce nanoribbons with the same shape as the masks. On the other hand, when nanowires with a cylinder shape are used, by the oxygen plasma etching, we can obtain nanoribbons thinner than the diameter of the nanowires, due to the smaller

contact area and the isotropic nature of the chemical reaction (Figure 2.6a). Furthermore, it has also been pointed out that there is less edge roughness in the nanoribbons made by nanowire masks than the ones made from EBL process.[82] Based on the above facts, nanowire masks and oxygen plasma etching are chosen for our BL-GNR devices.
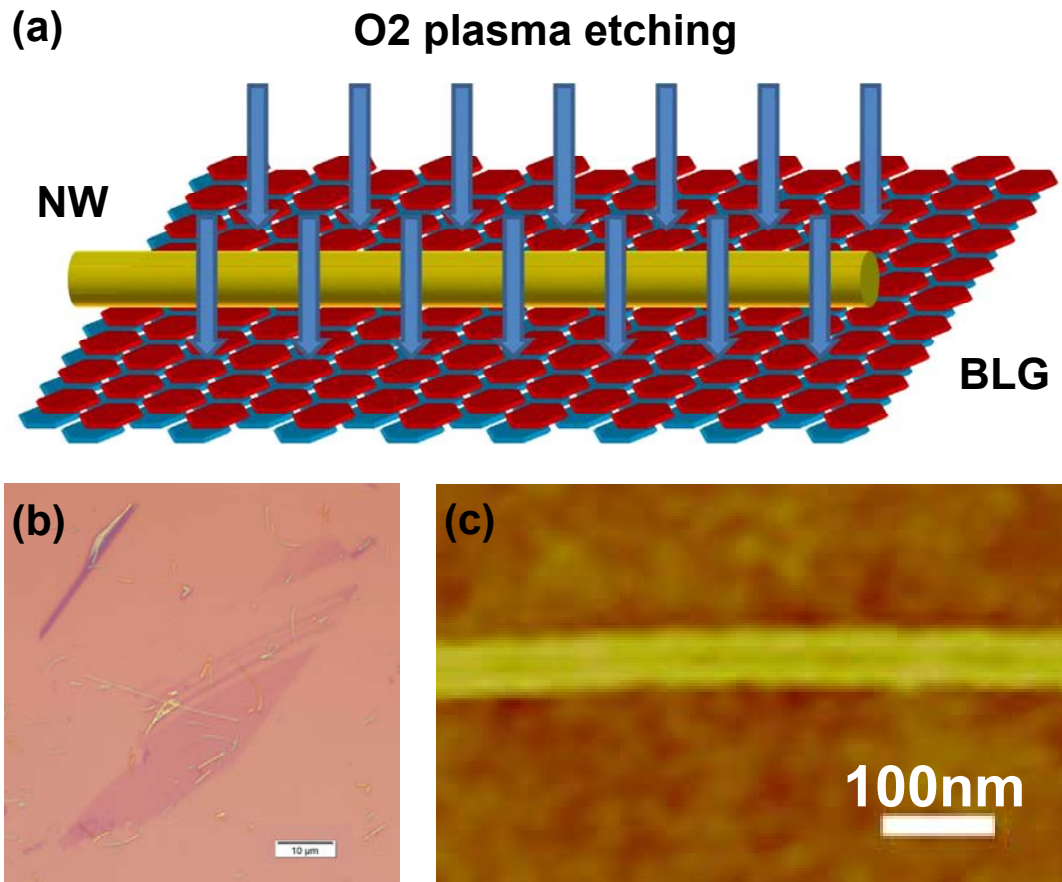
Figure 2.6 Etching BL-GNRs by nanowire masks and oxygen plasma. (a) Schematic of the etching process. (b) Microscope picture of silicon nanowires on a bilayer graphene film. The scale bar is 10 μm. (c) AFM image of a typical etched BL-GNR (~50 nm in width). The scale bar is 100 nm.

The process for transferring nanowires onto the existing bilayer graphene films is similar to the mechanical exfoliation (Figure 2.6b), which is also not well controlled and largely depends on experience and practice. The etching is done with the following parameters: 10 millitorr oxygen, 50 Watts RIE power, 10 seconds. Typical etching result is shown in Figure 2.6c.

2.4 Top-gate fabrication

To fabricate dual-gated devices, the top gate dielectrics need to be deposited on BL-GNRs. High quality high-κ dielectrics (Al_2O_3, HfO_2, etc.) are usually grown by atomic layer deposition (ALD) process. The ALD process relies on the chemical reactions between the substrate surface and selected chemicals, which is usually inhibited by the inert natural of the graphene surface. Hence the attempts to directly grow ALD dielectrics end up with nothing on the graphene films/GNRs. Different methods have been developed to solve this problem. Evaporated gate materials (e.g. SiO_2) have been used,[46] but usually suffer from high leakage currents. Polymer coating followed by the ALD growth is a better choice preferred by several research groups,[51] yet the gate stack is more complicated for the analysis. In our study, a thin layer of aluminum (~1.2 nm) is first evaporated on the Bl-GNRs at room temperature. Although pin-holes tend to form under this situation, the following ALD steps will oxide the aluminum first and use it as nuclei centers for the chemical reactions. This method has been developed to create tunneling junctions between graphene/metal interface,[31, 105] and also used by other groups for top gates on graphene films.[106] The resulting Al_2O_3 films on our BL-GNRs are

of good quality in terms of the permittivity, the void percentage, the leakage current density and the break down voltage.

2.5 Measurements

For the purpose of characterizing the transport properties, the measurements are conducted under pumped liquid helium temperature (1.7 K) to minimize the thermal energy. Both the low temperature Dewar from AMI Inc. and the physical properties measurement system (PPMS) from Quantum Design Inc. have been used. Electrical measurements were conducted using a standard low frequency lock-in setup (f < 1k Hz, δV_{ac} ~ 100 μV). (Unless stated otherwise, e.g. for temperature dependence measurements).
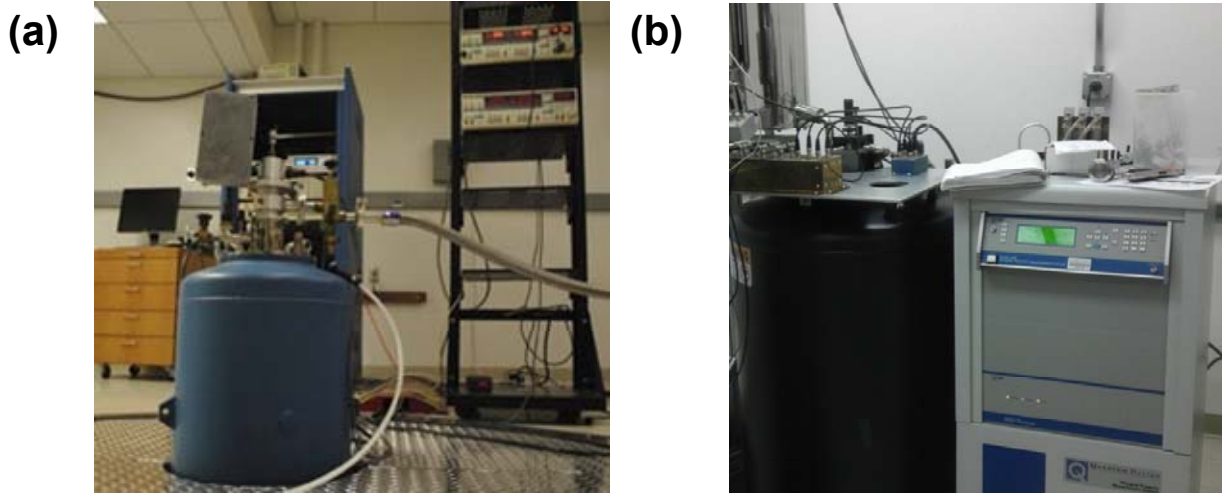
Figure 2.7 Measurement setups. (a) Low temperature Dewar from AMI Inc. (b) PPMS from Quantum Design Inc.

2.6 Summary

In this chapter, the fabrication process and the measurement setups for our BL-GNR devices are described. A-B stacking bilayer graphene films were obtained by the mechanical exfoliation method on highly doped Si substrate with 300 nm thermal SiO_2. Micro-Raman spectroscopy was used to identify the layer number and the stacking order. BL-GNRs were etched by oxygen plasma using transferred silicon nanowires masks. The top gate dielectrics were deposited with a thin layer of aluminum evaporation followed by ALD Al_2O_3 growth. All the electrodes were fabricated by EBL and standard lift-off process with Ti/Au. The electrical measurements were conducted at pumped liquid helium temperature using the standard low frequency lock-in setup.

Special attentions were paid for certain steps to improve the yield and avoid complications in the analysis. This process is not a very efficient one, but it has well served the purpose of understanding the transport properties of BL-GNRs.

Chapter 3

Transport properties of back-gated bilayer graphene nanoribbons

The first type of devices investigated in this study is the back-gated bilayer graphene nanoribbon (BL-GNR) on 300nm thermal silicon oxide (SiO_2) with highly doped silicon substrate as back gate electrodes (Figure 3.1a). Even though the thickness of the dielectric is far from the standard of industrial requirements, because of the fabrication process used at current stage (discussed in Chapter 2), this structure is the most straightforward choice. The AFM scan of a typical BL-GNR made from the nanowire etching masks is also shown in Figure 3.1b.
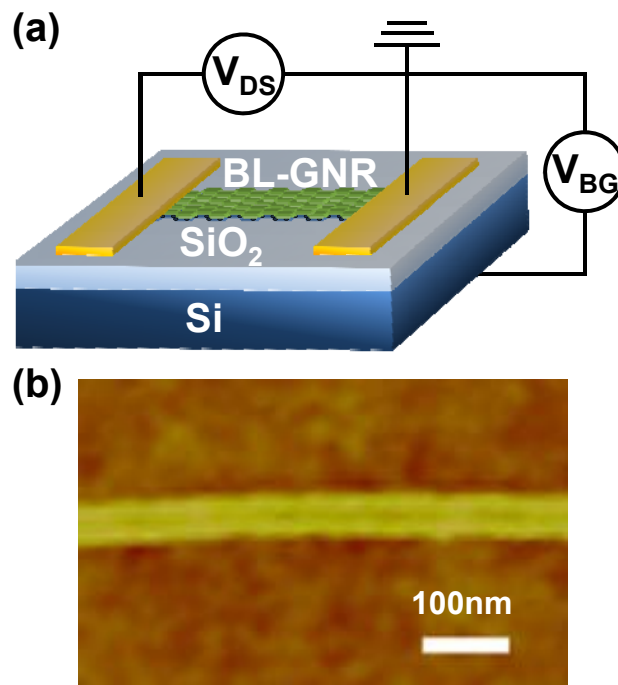
Figure 3.1 Back-gated BL-GNR device. (a) Device structure of a back-gated BL-GNR and the schematic of the measurement setup. The source-drain contacts are Ti/Au. The

thickness of the SiO$_2$ is 300 nm, and the degenerately doped (>2 × 10^{19} cm^{-3}) silicon substrate is used as back gate electrodes. (b) AFM image of one of the fabricated BL-GNRs using nanowire masks. The width of this BL-GNR is 50 nm (scale bar: 100 nm).

3.1 Energy Gaps in Bilayer Graphene nanoribbons

As a confined electronic system, energy gaps are expected in BL-GNRs. Gap-like behavior is indeed observed in the measurement. Figure 3.2 is a typical differential conductance (G ≡ dI/dV$_{DS}$) map as a function of both the back-gate modulation (V$_{BG}$) and the source-drain bias (V$_{DS}$). It is clear that a gapped region (blue or nearly blue color) extends in both horizontal and vertical directions. The analysis of this region reveals the basic transport properties of BL-GNRs.
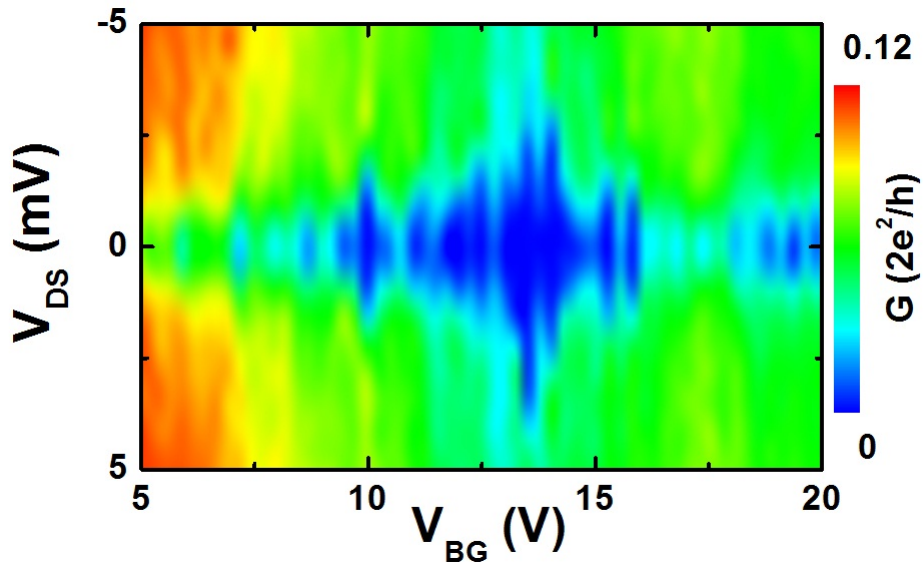
Figure 3.2 Typical G Vs V$_{BG}$ and V$_{DS}$ map measured from back-gated BL-GNRs. Gapped region with nearly zero conductance (blue region) observed within certain V$_{BG}$ and V$_{DS}$ ranges.

31

3.1.1 Gap-like behavior in BL-GNRs

At low temperatures, the energy band diagram can be probed using differential conductance measurements by applying a small δV_{ac} and setting V_{DS} = 0V. This corresponds to the trace along the center line in the map of Figure 3.2. The obtained G ~ V_{BG} curve is presented in Figure 3.3a. (At elevated V_{DS}, the energy profile of the device is modified by the lateral electrical field, so is the conductance behavior, Figure 3.3a inset). It is worth mentioning that the smooth method suggested by literature[70] has been adapted to remove the very dense oscillation peaks both inside and outside the gapped region. This smoothing method helps to resolve the properties of BL-GNRs from a large gate-voltage/energy range. Detailed analysis of the oscillation peaks will be presented later.

From the curve in Figure 3.3a, the overall behavior of the BL-GNR includes the highly suppressed conductance in the gapped region (from V_{BG} = 10 V to 16 V in this ribbon) and the highly repeatable oscillation peaks within. Based on the band structure of bilayer graphene[40], this gap in the energy scale can be calculated using the following equation:

$$\Delta E_{TR} = \frac{\hat{C}_{BG} \Delta V_{BG} \pi \hbar^2}{2m^* e} \qquad \text{(Eq. 3-1)}$$

where m^*(= 0.054m_e) is the effective mass near the Dirac point,[41] ΔV_{BG} (= 6 V) is the gap value in the voltage scale, and $\hat{C}_{BG}$ (= 1.04×10^{-21} F/nm^2) is the capacitance per unit area that takes into account the fringing effect for this nanometer size structure.[107, 108] The estimated gap is ΔE_{TR} = 87 meV for this particular BL-GNR.
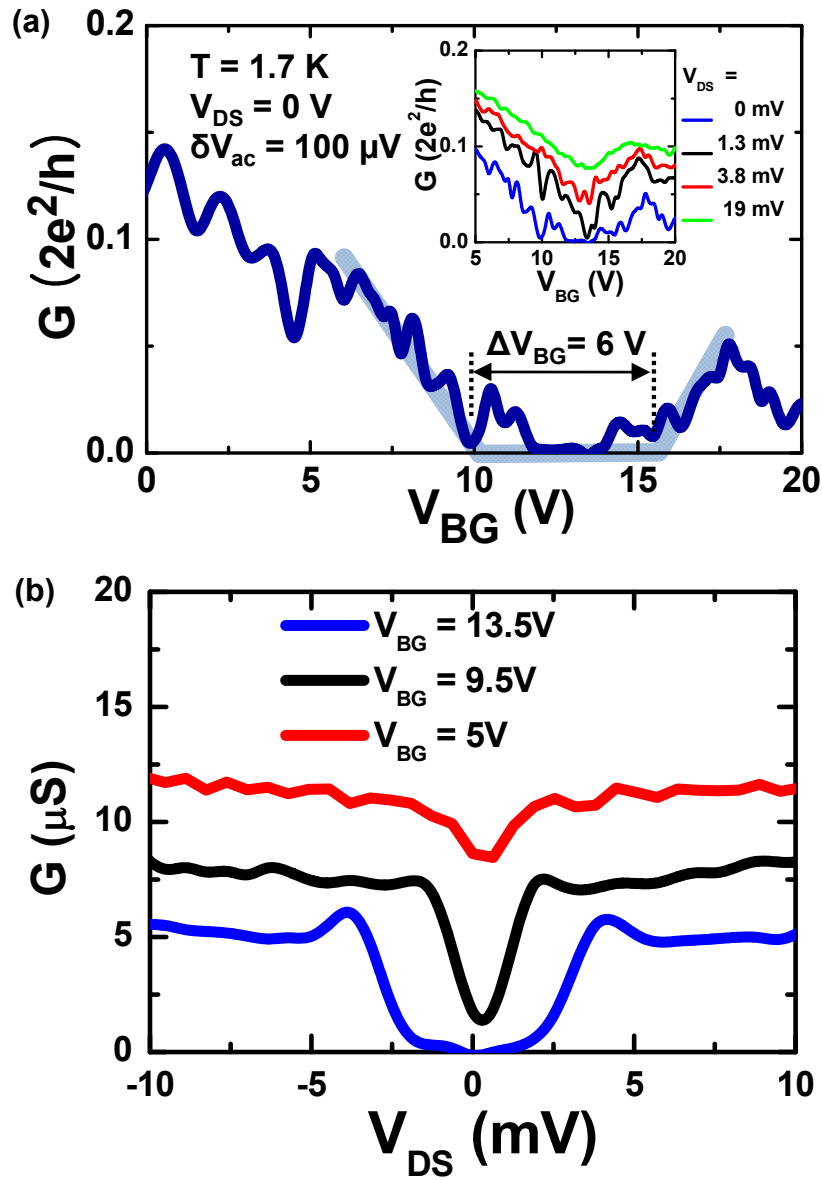
Figure 3.3 Gap-like behavior in BL-GNRs. (a) The conductance (G) dependence on the back-gate (V_{BG}) modulation at zero source-drain DC bias ($V_{DS} = 0$ V). Between V_{BG} = 10V ~ 16V (ΔV_{BG} = 6 V), G is strongly suppressed with repeatable resonance peaks. The corresponding transport gap is ΔE_{TR} = 87 meV. Inset: G ~ V_{BG} curves at different

V_{DS} biases. The gap-like behavior disappears at elevated source-drain biases. (b) G ~ V_{DS} curves at different back-gate voltages. Gap-like behavior (blue curve) can be observed when V_{BG} is set within the transport gap region.

3.1.2 Theoretical gaps in BL-GNR

To properly understand the transport properties, it is necessary to theoretically estimate the energy gaps and to compare with the measurement results shown above. In the BL-GNRs, the quantum confinement is one of the possible reasons for energy gaps. As mentioned before, the detailed value of the confinement gap in a graphene nanoribbon system highly depends on its edge configurations.[7] As a result, in our experiment, without the control of both the edge type and consistency, the accurate number cannot be obtained. However, an estimation of this gap can be acquired through basic quantum mechanics using the following equation:

$$\Delta E_{gC} \sim \frac{\pi^2 \hbar^2}{m^* w^2}$$ (Eq. 3-2)

where ΔE_{gC} is the confinement energy gap and w (~ 50 nm) is the width of this BL-GNR. The estimated quantum confinement gap is ΔE_{gC} ~ 5.6 meV.

Another possible energy gap from the theoretical point of view in a BL-GNR is the field-induced gap (ΔE_{FD}),[41, 43] which is directly related to the perpendicular electric field across the two carbon layers. By adapting the method described in reference,[49] the vertical electric displacement field is ~ 0.18 V/nm near the Dirac point in our measurements, and the corresponding field-induced gap is ΔE_{FD} ~ 18 meV.

3.1.3 Transport gap and its origin

By comparison between the experimental results and the theoretical estimations, it can be seen clearly that $\Delta E_{TR} >> \Delta E_{gC} + \Delta E_{FD}$. This indicates the gap-like behavior of BL-GNRs is not only determined by the energy gaps but also by other factors in the system. Considering the similarities to the gap-like behaviors described in the single-layer graphene nanoribbons (SL-GNRs) literature,[69-71] we believe the observed insulating state originates from the transport gap induced by the disorders along the nanoribbon.

There are two main sources of disorders in the BL-GNR system: charge impurities and edge disorders. They can cause different effects on the transport behavior.

Charge impurities exist universally in graphene related electronic systems (e.g. SLG, BLG, SL-GNR and BL-GNR). They are mainly from the environment close to the graphene samples, including oxide charges near the substrate surface, trapped charges between the graphene-substrate interface, contaminations from the fabrication process and atmosphere absorptions. These charges can cause the surface potential fluctuation and induce the so-called 'electron-hole puddles' in a graphene film. When the Fermi level (E_F) is set close to the Dirac point, patches with extra electrons or holes scatter in the sample, according to the distribution of the charge impurities. The potential fluctuation and electron-hole puddles in both single-layer and bilayer graphene films have been directly observed by scanning tunneling microscopes (STMs),[58, 109, 110] as shown in Figure 3.4 (a) & (b).

(a)

(b)

8nm

E_d (meV) 50 ▭ -5
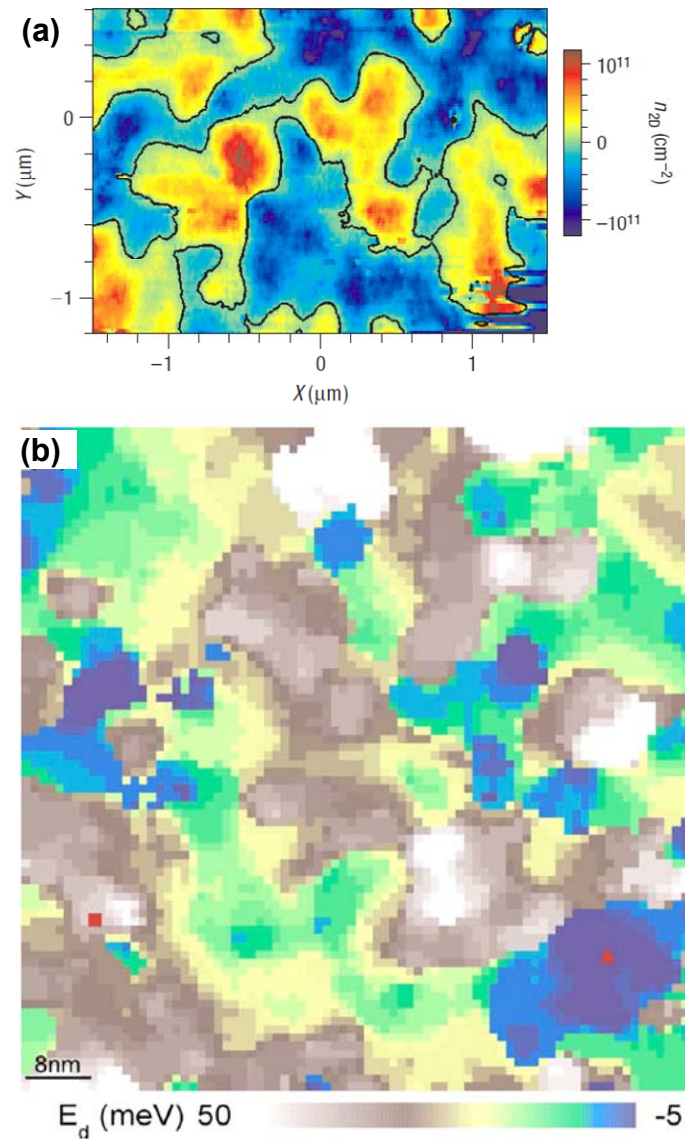
Figure 3.4 Surface potential fluctuation (electron-hole puddles) in single-layer and bilayer graphene films. (a) Spatial carrier density variation in a single-layer graphene film when the average carrier density is zero. The blue region represents electrons and the red region represents holes. [From J. Martin et al., Nat. Phys. 4(2), 144-148, 2008].[58] (b) Spatial variation of the surface potential of a bilayer graphene film. Both positive and negative shifts are observed, presented by different colors. Data are

extracted from the 2D differential conductance map from STM measurements. [From A. Deshpande et al., Appl. Phys. Lett. 95(24), 243509, 2009].[109]
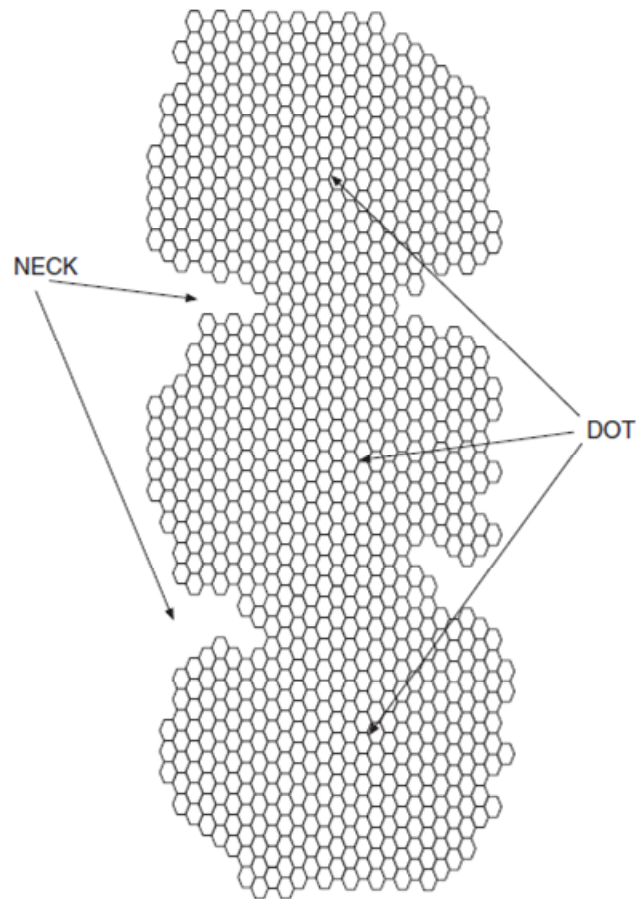
Figure 3.5 Schematic of quantum dots formed in a graphene nanoribbon from the edge roughness. The necks separated the quantum dots, causing Coulomb blockade effect in the carrier transport. [From F. Sols et al., Phys. Rev. Lett. 99(16), 166803, 2007].[62]

On the other hand, edge disorders are mainly from the graphene lattice. They have stronger effects on the nanostructures (e.g. SL-GNR and BL-GNR) than the large

scale samples. Due to the fabrication limitations, edge disorders in graphene nanoribbons are unavoidable at this stage, and have been observed in various forms (e.g. missing atoms, extra atoms, reformed edges and misalignments).[60, 61] In theoretical studies, several effects of edge disorders have been predicted. The first is to form quantum dots along graphene nanoribbons.[58, 62] As shown in Figure 3.5, when the size of the edge roughness is comparable to the width of the ribbon, single quantum dot or a chain of quantum dots can appear along the longitudinal direction, which mostly happens in extremely scaled cases. Another one is to induce localized edge states.[64, 111] These states can also contribute to the potential fluctuation of the whole graphene system, and change the local carrier density.[112] Oscillation peaks in conductance can also rise from the resonant between edge states, but these peaks are often randomly distributed rather than highly periodical compared to those from quantum dots.[63]

Both charge impurities and edge disorders exist in the bilayer graphene ribbons at the same time.[109, 113] Their contributions to the transport properties can be revealed from the detailed analysis of the measurement results.

3.2 Quantum dot behavior in bilayer graphene nanoribbons

To gain more information about the transport properties of BL-GNRs and the effects of the disorders, we zoom into the gapped region and take a closer look at the oscillation peaks.

3.2.1 Coulomb diamonds and Coulomb oscillations

From the colored conductance map shown in Figure 3.6, Coulomb diamonds are clearly resolved within this small back-gate modulation range. The periodicity of the Coulomb diamonds suggests it is unlikely to result from the resonance between the localized states,[69] but a strong indication of the existence of quantum dots in our BL-GNR.
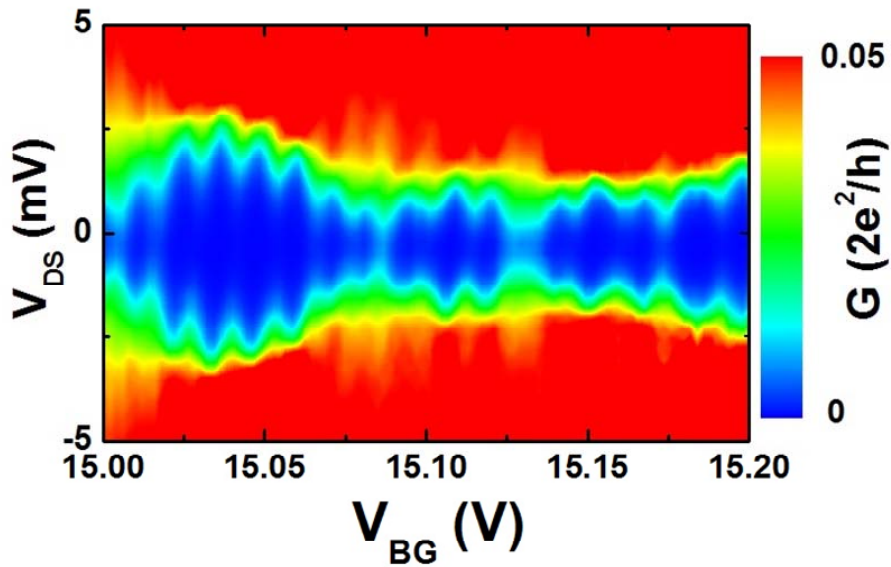
Figure 3.6 Color map: conductance versus V_{BG} and V_{DS}. The periodic Coulomb diamonds indicate the quantum dot nature of the BL-GNR.

In the context of quantum dots, a lot of information can be obtained from the detailed analysis of these Coulomb diamonds.[114] The charging energy of the quantum dot is estimated to be $E_C \sim 1.6$ meV and the back-gate lever arm $\alpha = C_G/C_{Total} \sim 0.1$, where C_G is the back-gate capacitance and C_{Total} is the total coupling capacitance

connected to the quantum dot. These numbers are later used to estimate the size of the quantum dot (session 3.2.3).

If the source-drain bias V_{DS} is set to zero, the Coulomb oscillation peaks can be observed on the $G \sim V_{BG}$ curve (see Figure 3.7). These peaks represent the Coulomb blockade effect, which dominates the transport properties of a quantum dot. According to the quantum dot theory,[114] the Coulomb oscillation peaks can be fitted by the following equation:

$$G \propto cosh^{-2}\left[\frac{e\alpha_G(V_{BG} - V_{Peak})}{2.5k_BT_{e(th)}}\right] \qquad \text{(Eq.3-3)}$$

Where α_G is the back gate lever arm extracted from the Coulomb diamonds, V_{Peak} is the voltage corresponding to the peak conductance, k_B is the Boltzmann constant and $T_{e(th)}$ is the electron temperature in the system.
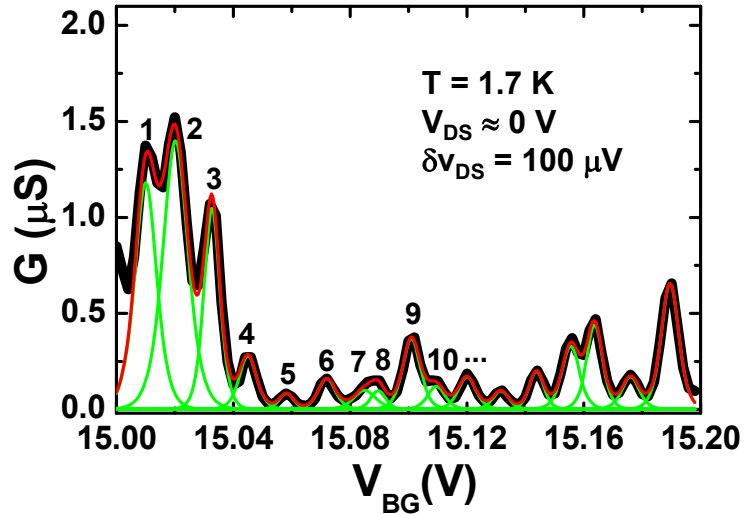
Figure 3.7 Periodic Coulomb oscillation peaks. Every single peak is fitted (green lines) by the equation $G \sim cosh^{-2}[e\alpha^{BG}(V_{BG}-V_{peak})/2.5k_BT_{e(th)}]$, where the sum (red line) of

all peaks matches the measurement data (black line) very well. The peak number (1, 2, 3…) is labeled to help extracting the peak spacing (see Figure 3.10).

Through adjusting $T_{e(th)}$ and V_{Peak}, all the oscillations can be fitted by Eq. 3-3. As shown in Figure 3.7, the sum of the fitted single peaks (red curve) accurately reproduces the measurement results (black curve). This not only corroborates the quantum dot nature of our BL-GNR, but also provides the accurate values of the peak position and the electron temperature ($T_{e(th)}$ = 2.1±0.5 K).

3.2.2 Origin of the quantum dots in BL-GNRs

From the Coulomb diamonds and the periodical Coulomb oscillations, the existence of quantum dots is confirmed in our BL-GNR devices. In order to further understand the behavior of the quantum dots and their effects on the transport property, it is necessary to find out the origin of such a structure in BL-GNRs.

The first possible source is geometrical confinement. In fact, in several literatures, specially designed single-layer and bilayer quantum dots have been achieved with electron beam lithography and oxygen plasma etching by several other research groups.[65, 115, 116] In such cases, the source and drain barriers have very different sizes comparing to the quantum dots. It also has been illustrated theoretically that in highly scaled graphene nanoribbons, edge disorders can cause the formation of the quantum dots.[62] In our BL-GNR, however, as seen from the AFM image presented

in Chapter 2 (Figure 2.6), no such constrains can be observed. So we exclude the geometrical effects.

(a)

(b)
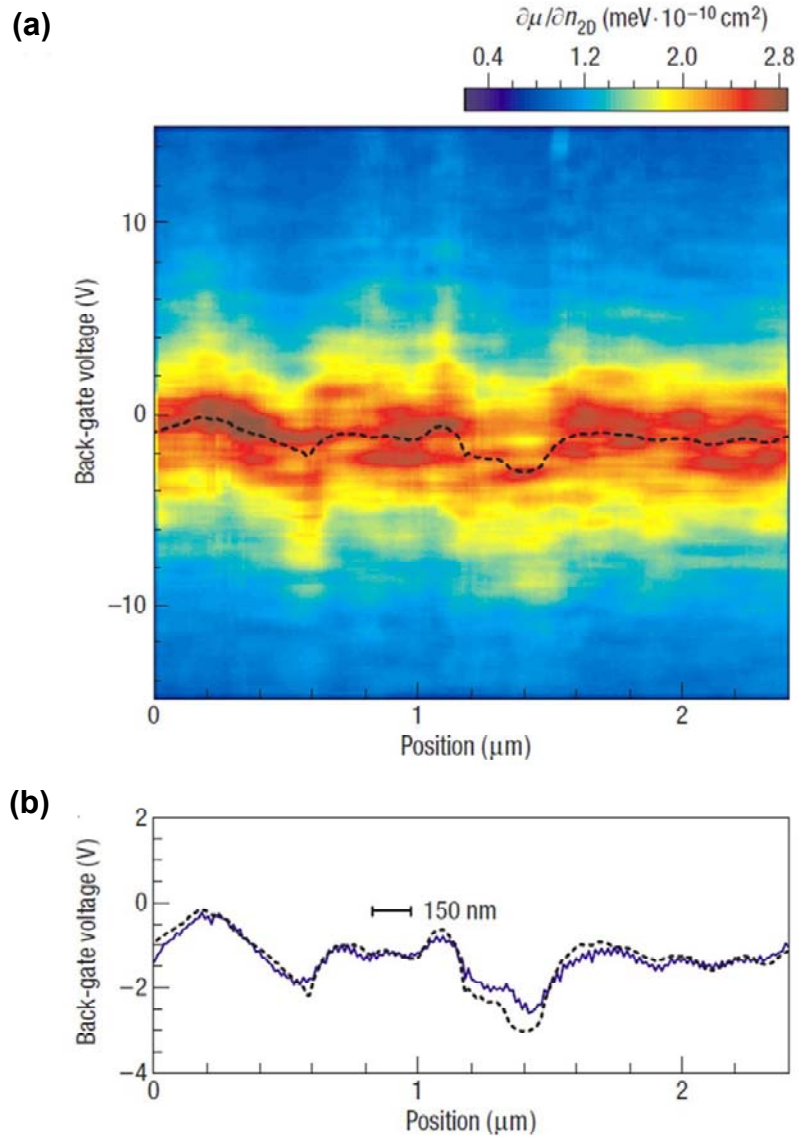
Figure 3.8 Potential landscape along a line cross a graphene sample. (a) the inverse compressibility measured by a scanable single-electron transistor (SET). The back dash line represents the position of the Dirac point determined by the kinetic energy fitting. (b) The position of the Dirac point from (a) comparing to the simple

subtraction method between surface potential at different back-gate bias. [From J. Martin et al., Nat. Phys. 4(2), 144-148, 2008].[58]

Alternatively, the source-drain barriers of a quantum dot can be created by tunneling junctions or PN junctions. As mentioned in session 3.1.3, disorders in bilayer graphene film can cause surface potential fluctuation, and form electron-hole puddles. Once we focus on a single line, this surface potential fluctuation becomes a potential landscape (see Figure 3.8).

This phenomenon also presents in the lateral confined graphene nanoribbons. Depending on the relative position between the potential landscape and the Fermi level of a BL-GNR, PN junctions will form along the carrier transport path. The portion between each adjacent PN junction pair can be considered as a quantum dot. As a result, each BL-GNR can be treated as a chain of quantum dots. Since electron-hole puddles are randomly distributed in bilayer graphene, the number and size of quantum dots in BL-GNRs also have large variations.

In our BL-GNR, the periodic Coulomb blockade oscillations exclude the picture of a multi-dot system consisting of various dot sizes although multi-dot behaviors are detected in other BL-GNR samples. In a multi-dot configuration, if the dots are exactly identical in size and potential profile, we would observe the same periodicity. This is because for each dot a slight difference in size and potential would lead to different charging energies (size) and S/D barriers (potential profile) and cause peak splitting upon gate modulation and/or temperature increase. However, the chance of having

identical dots along the width and/or along the channel is extremely low. Thus, we believe that the data represent a single dot configuration. According to the quantum dot literature,[117-119] this can further be confirmed by measuring the temperature dependence of the oscillation peaks (Figure 3.9). As the temperature is decreased, no splitting is observed in the periodic conductance peaks, but only a parallel shift of the peak positions occurs. The peaks become sharper with decreasing temperature as the thermal broadening of the carrier distribution function reduces. This corroborates the fact that our bilayer graphene nanoribbon is operating in a single quantum dot regime within the measured V_{BG} range.
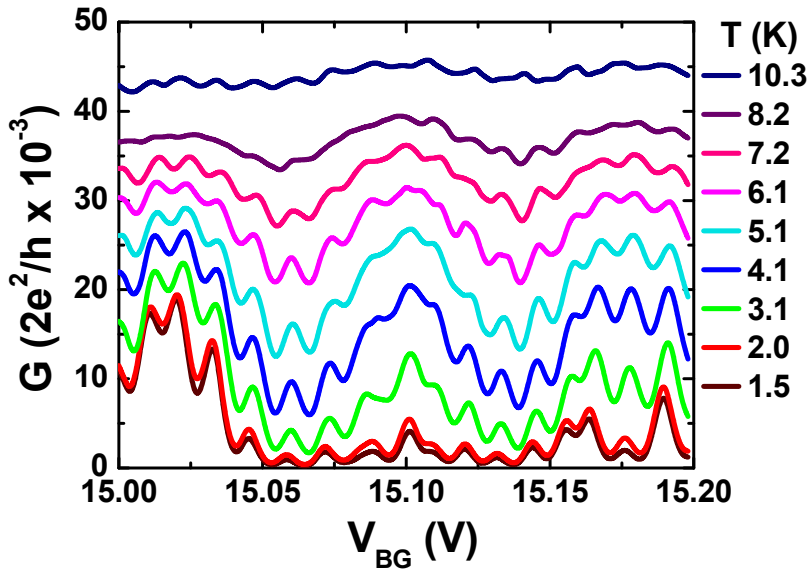
Figure 3.9 Periodic Coulomb oscillation peaks at different temperatures. With decreasing temperature, the peaks do not split, but shift parallel. The peaks become sharper at lower temperature because the thermal broadening reduces. This indicates that the BL-GNR is operating in the single dot regime within the measured V_{BG} range.

3.2.3 Size of the quantum dot

In a quantum dot system, the dimension information is of most importance among the basic parameters. The size of a quantum dot not only determines the energy splitting, but also directly relates to the capacitance coupling to the environment. And these two values together decide the energy/voltage needed to charge/discharge the dot with one extra electron during the measurements.[114] Following the same logic, by measuring the charging voltage and calculating the coupling capacitance, the size can be extracted for a given quantum dot.

According to the classical Coulomb blockade theory, the diameter of a disk-shaped quantum dot can be determined by the following equation:[71]

$$d = \frac{e^2}{4\varepsilon\varepsilon_r E_C} \qquad\qquad\qquad \text{(Eq.3-4)}$$

Where E_C is the charging energy, ε is the vacuum permittivity and ε_r ($= (\varepsilon_{air} + \varepsilon_{SiO2})/2$) is the relative permittivity of the surrounding dielectrics. Based on this model, the diameter of the quantum dot in this BL-GNR is estimated to be ~ 1µm, which is much larger than the whole dimension of the ribbon. The overestimation of the size clearly indicates that the disk-shaped model is not suitable for the quantum dot within the BL-GNR.

An alternative way to calculate the size of a quantum dot is based on the following relationship:[114]

$$\delta V_{BG} = \frac{1}{e\alpha_G}\left(\Delta E + \frac{e^2}{C_{dot}}\right) \qquad\qquad\qquad \text{(Eq.3-5)}$$

Here, $\delta V_{G\backslash BG}$ is the voltage spacing between Coulomb oscillation peaks, α_G is the back gate lever arm, ΔE is the energy splitting and C_{dot} is the total capacitance of the quantum dot. In the case of our BL-GNR, a larger dot size and small energy splitting are expected, so Eq. 3-5 can be simplified to:

$$\delta V_{BG} \approx \frac{1}{e\alpha_G} \times \frac{e^2}{C_{dot}} = \frac{e}{C_{BG}} \qquad \text{(Eq.3-6)}$$

The relationship between back-gate capacitance $C_{G\backslash BG}$ and total capacitance C_{total}, C_{BG} = $\alpha_G \times C_{dot}$ is used in the above simplification. After finding δV_{BG} from the linear fit of the peak positions (see Figure 3.10), the gate capacitance C_{BG} can then be estimated by Eq. 3-6. Based on the device structure of this BL-GNR (w ~ 50nm, d_{SiO2} ~ 300nm), the gate capacitance per unit length $\hat{C}_{BG}$ including fringing effect can be calculated analytically using a method given in reference 108. Finally, we divide C_{BG} by $\hat{C}_{BG}$ to obtain the size of the quantum dot.

As can be seen in Figure 3.10, the fitting of the peak positions give two different peak spacing values (δV_{BG1} ~ 12.65 mV, δV_{BG2} ~ 11 mV), each corresponding to a back-gate capacitance value (C_{BG1} = 1.26×10^{-7}F, C_{BG2} = 1.45×10^{-7}F). Using the method described above, we find a 15% increase of the dot size from 12150nm^2 (50nm × 243nm) to 14000nm^2 (50nm × 280nm) upon increasing the back-gate voltage. This effect can be explained by the potential landscape model as illustrated in Figure 3.11. The increase of the back-gate voltage not only increases the number of electrons in the quantum dot but also gradually shifts the Fermi level (E_F) to a higher energy level relative to the potential landscape. When E_F is located at position I (bottom), the

quantum dot size is relatively small and results in a large δV_{BG1}. When E_F moves to position II (top), the quantum dot becomes larger with a smaller δV_{BG2}.
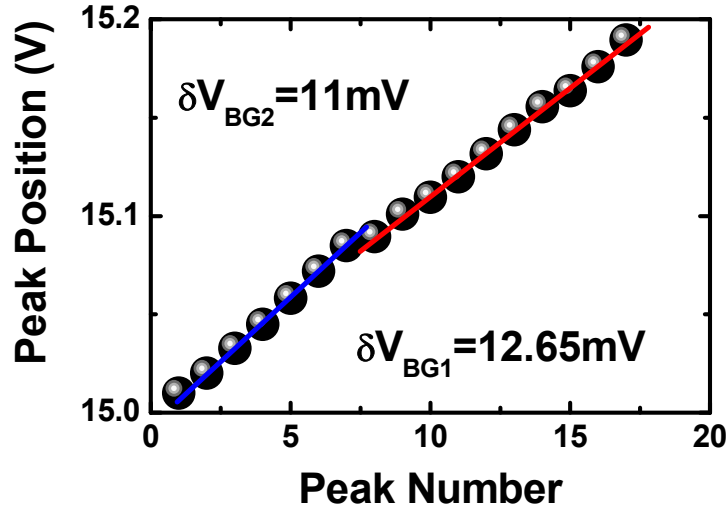
Figure 3.10 Peak position versus peak number for the Coulomb oscillations in the BL-GNR. Peak positions (voltages) obtained from the single curve fittings in Figure 3.7. From the linear fittings, two different values of the peak spacing are extracted δV_{BG1} = 11mV and δV_{BG2} = 12.65mV, corresponding to two different quantum dot sizes within the studied back-gate range: 14000 nm^2 (50 nm × 280 nm) and 12150 nm^2 (50 nm × 243 nm).

Based on this model, the quantum dot in our BL-GNR has a rectangular shape with a certain aspect ratio instead of a disk shape. This is decided by the natural shape of nanoribbons. Since the quantum dot takes over the whole width of the ribbon, the variation in size is mainly from the length. In fact, in the case of the SL-GNRs, single quantum dots with similar aspect ratios are also reported.[69]
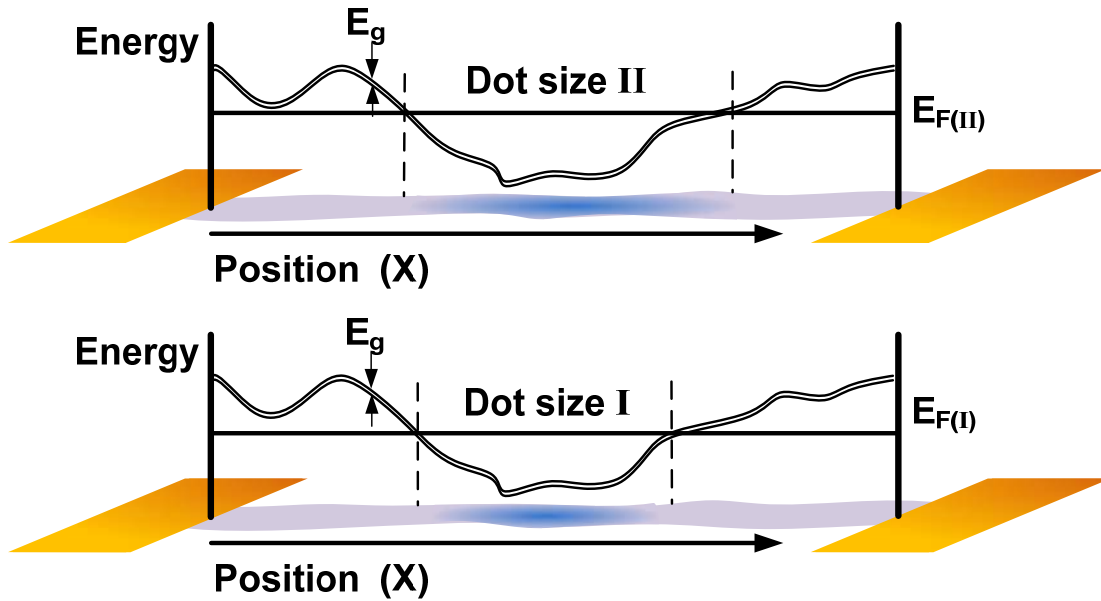
Figure 3.11 Illustration of the change in quantum dot size. Upon modulation of the E_F by V_{BG}, the quantum dot becomes larger with smaller peak spacing δV_{BG2} at $E_F(II)$ compared to peak spacing δV_{BG1} at $E_F(I)$. (E_g is the combination of the confinement gap and the field-induced gap.)

3.2.4 Stability of the quantum dots

Another important property of a quantum dot is its stability. It measures how the source-drain barriers react to external disturbances, including thermal fluctuations and excessive energies. For the spontaneously formed quantum dots in our BL-GNRs, this reflects the stability of the potential landscape against these external influences. The stability can be quantified by electron temperatures in a quantum dot system.

In case of the thermal stability, the electron temperature $T_{e(th)}$ can be extracted in the single Coulomb oscillation peak fitting using Eq. 3-3. As mentioned before, for all the peaks, $T_{e(th)}$ has a value ~2.1K with small variations (see Figure 3.7), nearly identical to the measurement temperature 1.7K, which proves that the source-drain barriers of the quantum dot (from the potential landscape) are stable against thermal fluctuations.
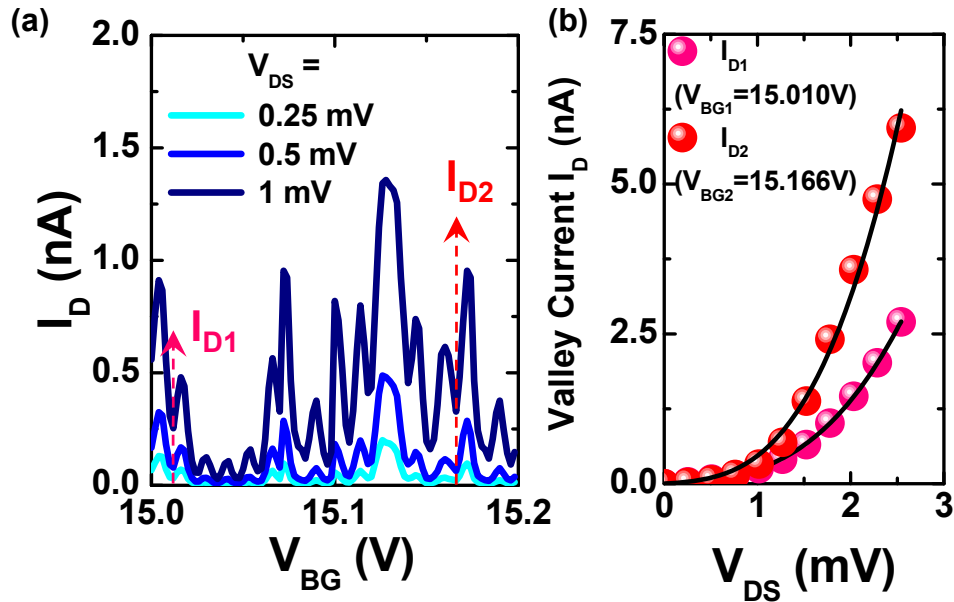
Figure 3.12 Co-tunneling and stability of the quantum dot in BL-GNR. (a) Current versus V_{BG} at various V_{DS}. The valley current at the Coulomb blockade state increases with V_{DS}. The arrows indicate the Coulomb blockade state shown in panel b. (b) Valley current depending on V_{DS}. The effective electron temperature of $T_{e(ex)} < 2K$ is obtained, which is nearly identical to the measurement temperature (1.7 K). This indicates that the potential profile of the source/drain barriers remains stable at different biases.

Beside temperature change, excessive energies also can be applied to the quantum dots (e.g. by increasing the source-drain bias).[120-122] This will cause the co-

tunneling effect in the quantum dots and raise the valley currents between Coulomb oscillation peak. According to the quantum dot theory,[120, 121] the dependence of the valley current on the applied source-drain bias can be characterized by the following equation:

$$I_D = aG_S G_D\left[(eV_{DS})^2 + \left(2\pi k_B T_{e(ex)}\right)\right]V_{DS}$$
(Eq.3-7)

Where a is the proportional factor, G_S and G_D are the source and drain conductance, and $T_{e(ex)}$ is the effective electron temperature relevant to excess energies.[120, 121] By fitting all the valley currents with the above equation (two examples shown in Figure 3.12b), we obtain $T_{e(ex)} < 2K$, which is also very close to the measurement temperature (1.7K) indicating the stability of the potential landscape against increased source-drain bias. Since the acoustic phonon scattering is negligible at T = 1.7K, the slight discrepancy may be ascribed to electron-electron interactions.

The stability of the spontaneously formed quantum dots in BL-GNRs points to a potential direction for applications. By intentionally fabricating local top-gates as source/drain junctions, electrically confined quantum dots may be achieved in bilayer graphene nanoribbons. These devices can be considered as promising candidates for single electron transistors (SETs).

3.3 Comparison with SL-GNRs

Finally we discuss several possible distinct properties of quantum dots in bilayer graphene nanoribbons compared to those of reported single-layer graphene nanoribbons, even though the potential fluctuations are responsible for both cases.[69, 71]

According to theoretical and experimental studies, bilayer graphene has a broader distribution function of the carrier concentration at the charge neutrality point (Dirac point) for the same amount of charge impurities than that of single-layer graphene (Table 1),[109, 123, 124] which indicates near the Dirac point, bilayer graphene tends to combine areas with different extra carrier densities to form larger puddles, while in single-layer graphene there are higher possibilities to find smaller patches with similar extra carrier densities. This assists a single dot formation along a wide and long bilayer graphene nanoribbon. In addition, the electric field-induced energy gap may further increase the tunnel resistance[41] and promote quantum dot formation in bilayer graphene nanoribbons compared to single-layer graphene nanoribbons.

Table 1 A comparison of the band structure, energy gaps, transport gaps, carrier and potential fluctuation and quantum dot size between SLG (SL-GNR) and BLG (BL-GNR). The values are taken from various literature and our current work.

	Dispersion relation near E_F	Confinement Gap	Field-Induced Gap	Carrier and Potential Fluctuation (experiment)[a]	Carrier and Potential Fluctuation (theory)[a]	Transport Gap	Quantum Dot Size
SLG	$E = \hbar k u_F$ (u_F ~10^6 m/s)[40]	$\Delta E \sim \hbar u_F/w$ (6.6 meV, w ~50 nm)[65]	N/A	Δn~ 2.3×10^{11} cm^{-2} (ΔE_d~ 50meV)[58]	Δn~ 1.2×10^{11} cm^{-2} ΔE_d~ 36meV (at n_{imp} = 1×10^{11} cm^{-2})[123]	100-200 meV (w ~50 nm)[72] >200 meV (w ~30 nm)[69, 70]	7850 nm^2 (w ~30 nm)[10] 3000 nm^2 (w ~30 nm)[9]
BLG	$E = \hbar^2 k^2/2m^*$ (m^* ~$0.054 m_0$)[41]	$\Delta E \sim \pi^2 \hbar^2/m^* w^2$ (~5.6 meV, w ~50 nm)†	2 meV ($D \approx 0.02$ V/nm)[49]	Δn~ 3.8×10^{11} cm^{-2} (ΔE_d~ 20meV)[109]	Δn~ 5.5×10^{11} cm^{-2} ΔE_d~ 29meV (at n_{imp} = 1×10^{11} cm^{-2})[123]	87 meV (w ~50 nm)‡	12150-14000 nm^2 (w ~50 nm)‡

The Δn is the standard deviation of the carrier density fluctuation; ΔE_d is the corresponding surface potential fluctuation, and n_{imp} is the charge impurity concentration. Although ΔE_d is smaller in BLG due to the screening effects, BLGs have a wider distribution function of the carrier concentration fluctuation (larger Δn) than SLG because of the difference in dispersion relation.[123] [b]Estimated value. [c]Experimental results.

3.4 Summary

In conclusion, we studied the transport properties of back-gated bilayer graphene nanoribbons fabricated using nanowire etching masks. The Coulomb diamonds inside the transport gap reveal the quantum dot nature of the bilayer graphene nanoribbon. The origin of the quantum dot is attributed to the disordered surface potential induced by charge impurities and/or edge roughness present along the nanoribbon. By extracting the effective temperatures related to thermal broadening and excess energies, we find that the potential landscape forming the quantum dot in bilayer graphene nanoribbons is stable under thermal fluctuations and energy perturbations. Our results lead to the conclusion that for the potential applications of BL-GNRs, the disordered surface potential fluctuations need to be reduced either by eliminating the charge impurities through the usage of suspended structures,[17] a hexagonal-BN sacrificial layer, and high-κ dielectrics[125, 126] or by minimizing the edge roughness utilizing a fabrication scheme with controlled edge roughness.[84, 127-130] Alternatively, the stability of the potential profile can be exploited by fabricating local top-gates for SET devices.

Chapter 4

Transport properties of dual-gated bilayer graphene nanoribbons

The field-induced energy gap (ΔE_{FD}) is one of the most intriguing properties of bilayer graphene.[41] In this chapter, the effects of ΔE_{FD} on the transport properties of bilayer graphene nanoribbons (BL-GNRs) will be discussed in detail. In order to create and control the perpendicular electric displacement field (D) across the graphene layers, dual-gated devices (see, Figure 4.1) are fabricated and measured using the process described in Chapter 2. Furthermore, to emphasize the different transport behaviors in different materials, the same structure is also applied to single-layer graphene, bilayer graphene and single-layer graphene nanoribbon devices which are all measured under the same condition.

4.1 Field-induced gap in electrical measurements

Unlike the optical methods,[47-49] it is hard to directly observe the field-induced gap in bilayer graphene samples through electrical measurements, owing to the unavoidable surface potential fluctuations. Near the charge neutral point (Dirac point), these potential fluctuations tend to smear the effective energy gap to a much smaller value than the actual ΔE_{FD}, so that the device resistance will not be high enough to block the current. On the contrary, in the case of optical measurements, this effect only increases the broadening of the resonance peaks but not their positions, which makes it possible to

identify the accurate energy. For this particular reason, an indirect indicator must be used to show the signature of the field-induced gap in electrical measurements.
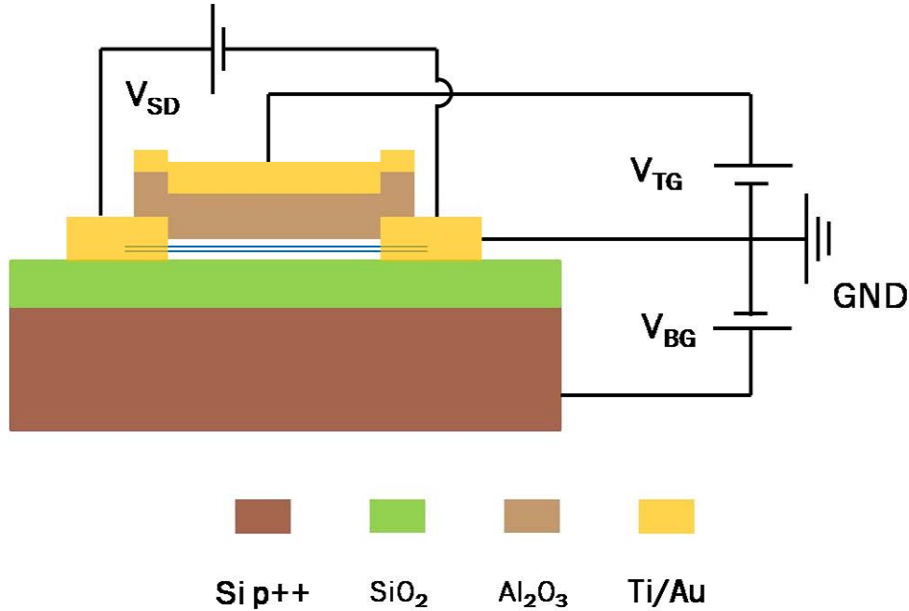
Figure 4.1 Schematic device structure and measurement setup of dual-gated BL-GNRs. The back-gate dielectric is a 300 nm thick thermally grown SiO_2. The top gate dielectric is an ALD grown Al_2O_3 layer (18 nm for BL-GNR G222C and 20 nm for G246K). A frequency of 1k Hz and an AC voltage of $\delta V_{DS} = 100$ μV are used for the lock-in measurements at 1.7 K.

4.1.1 Field-induced gap in bilayer graphene devices

To demonstrate the existence of the field-induced gap in our bilayer graphene samples, we first compare the measurement results from dual-gated bilayer graphene devices and single-layer graphene devices, as shown in Figure 4.2. On each R ~ V_{TG} curve, the resistance reaches its maximum value (R_{max}) at the charge neutral point,

indicating the carrier density here is adjusted to be zero by the modulation from both gates. On the energy diagrams, the Fermi level is right at the Dirac point of the single-layer and bilayer graphene film (at the center of the field-induced gap of the bilayer graphene film with a none-zero D field), as shown in Figure 4.2 (c), (d) & (e). The top-gate voltage at this point is defined as V_{TG}^{Dirac}.
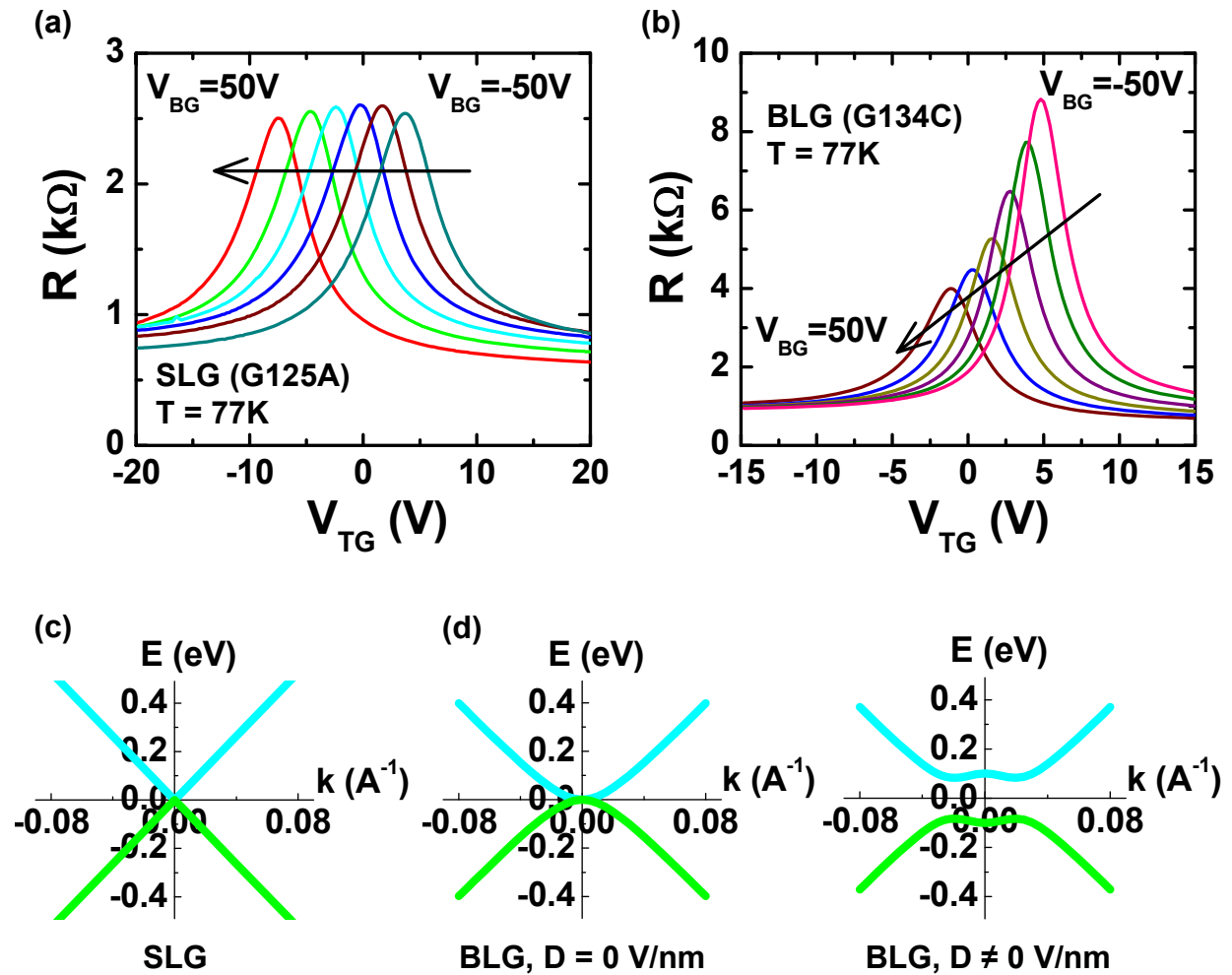
Figure 4.2 Signatures of ΔE_{FD} in bilayer graphene devices. (a) R ~ V_{TG} curves at different V_{BG} of a single-layer graphene device (G125A). R_{max} remains near constant while V_{TG}^{Dirac} moves with V_{BG}. (b) R ~ V_{TG} curves at different V_{BG} of a bilayer graphene

device (G134C). Both R_{max} and V_{TG}^{Dirac} change with V_{BG}. Measurements were conducted at T = 77K for both (a) & (b). (c) Band diagrams at the charge neutral points in single-layer graphene. (d) & (e) Band diagrams at the charge neutral point in bilayer graphene when the perpendicular electric displacement D = 0 V/nm (d) and D ≠ 0 V/nm (e). Only the low energy subbands are shown, and the potential difference between layers is set to 0.2 eV.

It is clear that in both single-layer and bilayer graphene, V_{TG}^{Dirac} has different values depending on V_{BG}. This can be easily understood from the capacitance-coupling point of view, where the carrier density can be calculated from the following equation:

$$\frac{Q_{tot}}{\varepsilon_0} = \frac{V_{BG} \times \varepsilon_{BG}}{d_{BG}} + \frac{V_{TG} \times \varepsilon_{TG}}{d_{TG}} + \frac{Q_0}{\varepsilon_0}$$ Eq.(4-1)

Here, Q_{tot} is the total carrier density, Q_0 is the carrier density at zero gate bias, d is the thickness of each gate and ε is the permittivity of the gate dielectric. At the charge neutral point ($V_{TG} = V_{TG}^{Dirac}$), Q_{tot} = 0. So

$$V_{TG}^{Dirac} = -\left(\frac{V_{BG} \times \varepsilon_{BG}}{d_{BG}} + \frac{Q_0}{\varepsilon_0}\right) \times \frac{d_{TG}}{\varepsilon_{TG}}$$ Eq.(4-2)

is a function of V_{BG}. This equation holds for both single-layer and bilayer graphene, in a similar fashion to the dependence of the threshold voltage on the doping concentration in regular semiconductor devices,[131] except that here the doping is controlled by V_{BG}. What is different is the behavior of R_{max}. R_{max} remains near constant in single-layer graphene devices, but changes drastically in bilayer graphene devices for different

56

back-gate voltages. The reason is the changes in the D field and the corresponding band structure modification in bilayer graphene. For a Given V_{BG}, the value of V_{TG}^{Dirac} can be calculated by Eq. (4-2). And the apparent electric displacement field at the charge neutral point (where $V_{TG} = V_{TG}^{Dirac}$) is

$$D = \frac{\left(V_{TG}^{Dirac} - V_{TG(0)}^{Dirac}/2\right) \times \varepsilon_{TG}}{d_{TG}}$$

Eq. (4-3)

where $V_{TG}^{Dirac}{}_{(0)}$ is the top-gate voltage of the charge neutral point when $V_{BG} = 0$ V. So the D field is also a function of the back-gate voltage. The changing of the D field does not affect the band structure of the single-layer graphene, except a parallel shift on the energy axes, so R_{max} will not change. But in the case of bilayer graphene, even though the Fermi level always stays at the center of the gap, the sizes of the gap are modulated greatly by D. Thus, the R_{max} increases with D (V_{BG}). The V_{BG} modulation of the R_{max} is a distinct signature of the ΔE_{FD} in bilayer graphene devices.[46]

Based on Eq. (4-1) and Eq. (4-2), the D field at the charge neutral point can also be calculated by the following equation, which gives the same results as Eq. (4-3),

$$D = \frac{\left(V_{BG}^{Dirac} - V_{BG(0)}^{Dirac}/2\right) \times \varepsilon_{BG}}{d_{BG}}$$

Eq. (4-4)

where $V_{BG}^{Dirac}{}_{(0)}$ is the back-gate voltage of the charge neutral point when $V_{TG} = 0$ V.

4.1.2 Field-induced gap in bilayer graphene nanoribbon devices

For the case of BL-GNRs, as aforementioned in Chapter 3, the transport gap (ΔE_{TR}) will be formed at low temperatures. Hence, it is impossible to find out the position

of V_{TG}^{Dirac} and the maximum resistance value. To compare with bilayer graphene devices, we first measure the BL-GNRs at liquid nitrogen temperature (77K), Figure 4.3a. The signature of ΔE_{FD}, i.e., the change of R_{max} with V_{BG}, remains in our BL-GNR devices, which indicates the field-induced gap still exists in the ribbon scale. As a reference, measurement results from a SL-GNR device are also plotted in Figure 4.3b. The key features have been inherited from single-layer graphene devices (i.e., V_{TG}^{Dirac} moves with V_{BG}, R_{max} remains near constant), only the resistance value drops owing to the reduced device width.
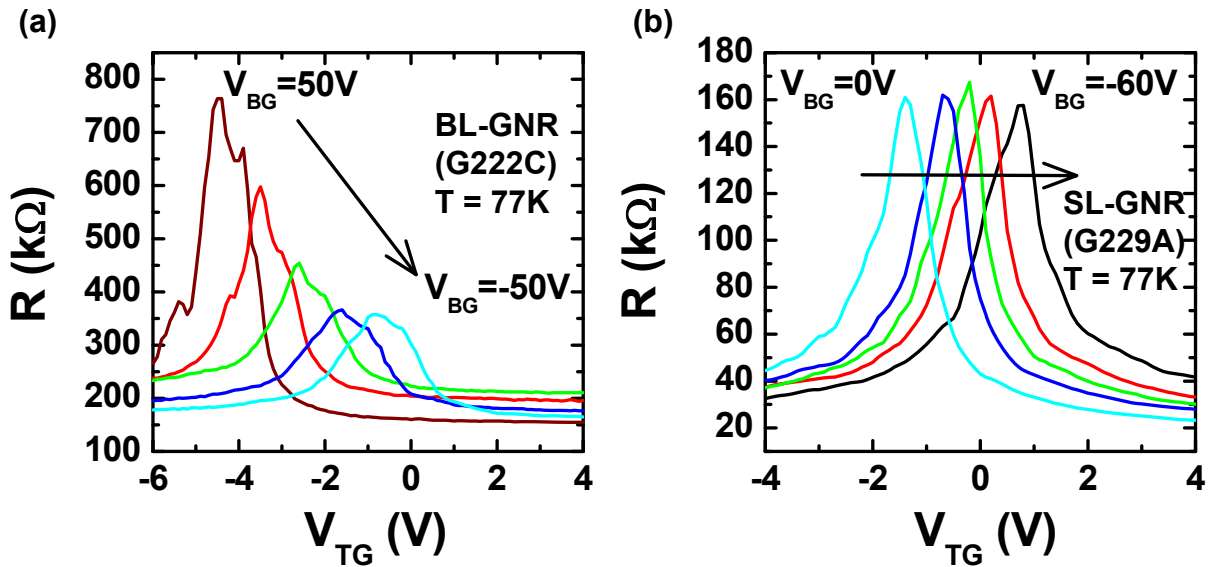
Figure 4.3 Signature of ΔE_{FD} in BL-GNRs. R ~ V_{TG} curves of a BL-GNR device G222C (a) and a SL-GNR device G229A (b) with different V_{BG} bias. Measurements were conducted at liquid nitrogen temperature (77K) to show V_{TG}^{Dirac} and R_{max} in the graphene nanoribbons.

4.2 Transport Gap (ΔE_{TR}) in dual-gated BL-GNRs
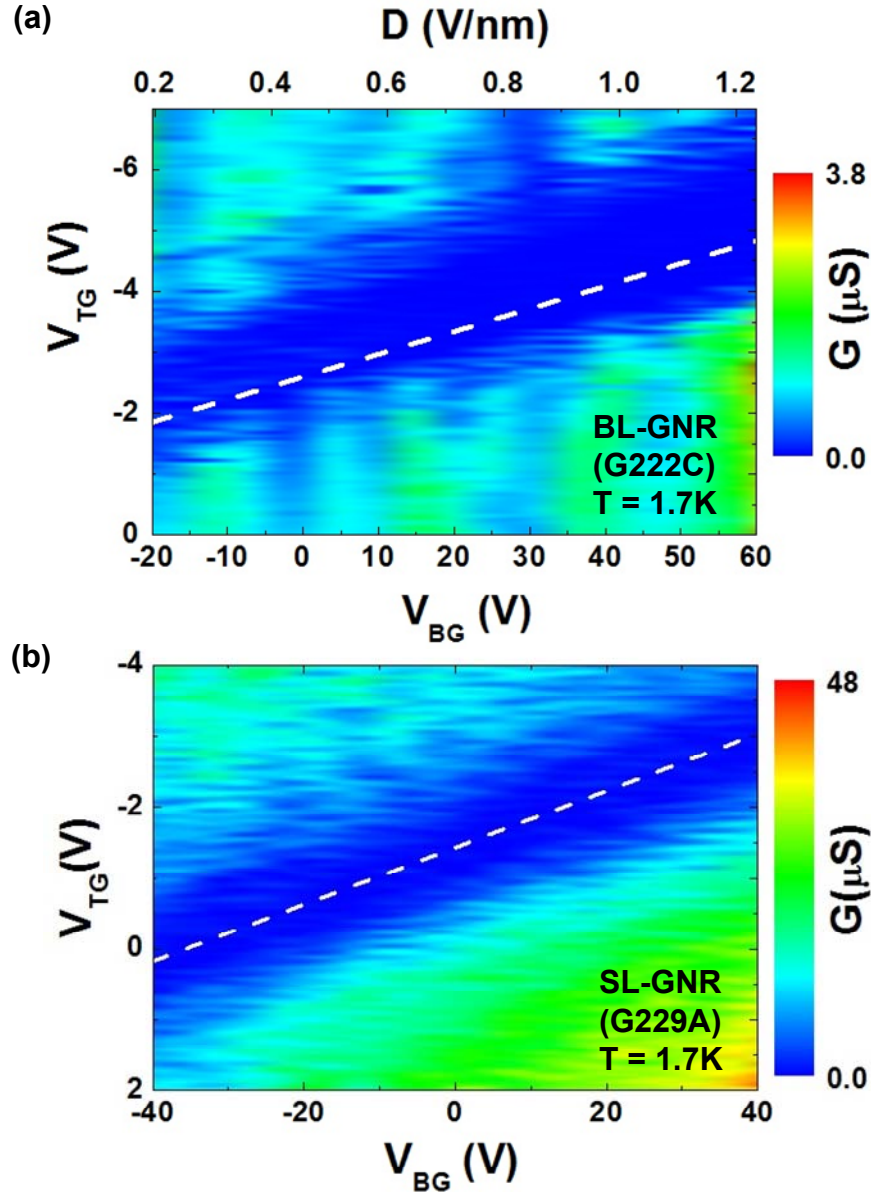
Figure 4.4 Conductance dependence on V_{BG} and V_{TG} in BL-GNRs and SL-GNRs.

(a) Typical measurement results from dual-gated BL-GNRs (G222C). The size of ΔE_{TR} increases with D field, while the oscillation peaks (spikes) reduce. The perpendicular displacement field D is calculated from Eq. 4-3. (b) Measurement results from a dual-gate SL-GNR (G229A). Both ΔE_{TR} and the oscillation peaks remain the same at

different V_{BG}. The white dash lines mark the measured V_{TG}^{Dirac} at different back-gate voltages. T = 1.7 K for both measurements.

After confirming the existence of ΔE_{FD} in BL-GNRs, we reduce the temperature to pumped liquid helium temperature (1.7K) and adjust both top-gate and back-gate to control the D field across the graphene layers. The typical conductance dependence on V_{TG} and V_{BG} at V_{DS} = 0 from our measurements is plotted in Figure 4.4a. For the purpose of comparison, similar measurement results from a dual-gated SL-GNR are presented at the same time in Figure 4.4b.

There are three observations that can be made from this color map. First, the position of the transport gap moves with V_{BG}. This is consistent with the fact that at higher temperatures, the position of V_{TG}^{Dirac} changes with the V_{BG} (Figure 4.3a), since the transport gap has to form around the V_{TG}^{Dirac}. And this also can be seen in the measurement results from the SL-GNR. Second, the gapped region in the top-gate direction changes its size at different V_{BG}. Third, the oscillations, represented by the small spikes within the blue (gapped) region also have different densities at different V_{BG}. The last two features cannot be found in the map from the SL-GNR. They are unique to dual gated BL-GNRs and they can only come from the coupling between the two layers.

4.2.1 Size of the transport gap

To quantify the dependence of the transport gap size on the electric field/field-induced gap, we extracted the value of the gap on the energy scale from each $G \sim V_{TG}$ curve by replacing $\hat{C}_{BG}$ and ΔV_{BG} with C_{TG} and ΔV_{BG} in Eq. 3-1. For comparison purpose, the estimated ΔE_{TR} is plotted in Figure 4.5 (blue dots) together with the values of the field-induced gap (ΔE_{FD}) obtained from reference 43 based on the density functional theory (DFT) calculation (red line).
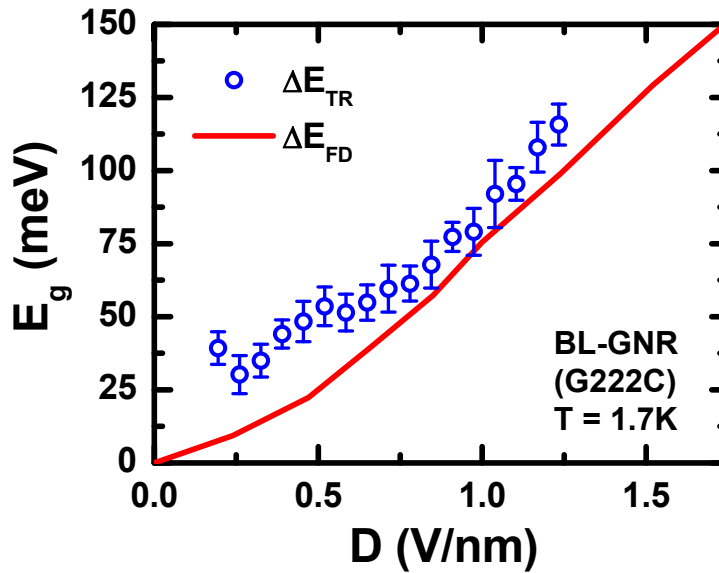
Figure 4.5 Transport gap and field-induced gap versus electric field in BL-GNRs. The values of the transport gap ΔE_{TR} (blue dots) are extracted from Figure 4.4a (BL-GNR G222C). The perpendicular displacement field is calculated using Eq. 4-3. The values of the field induced gap values ΔE_{FD} (red line) are from DFT calculation.[43]

From the plot, we can see that in the high field regime, ΔE_{TR} can be larger than ΔE_{FD}, and they both decreases with the D field. However, once the field reduces to around 0.6 V/nm in this device, ΔE_{TR} remains around 35 meV while ΔE_{FD} continues dropping to zero.

4.2.2 Oscillation peaks within the transport gap
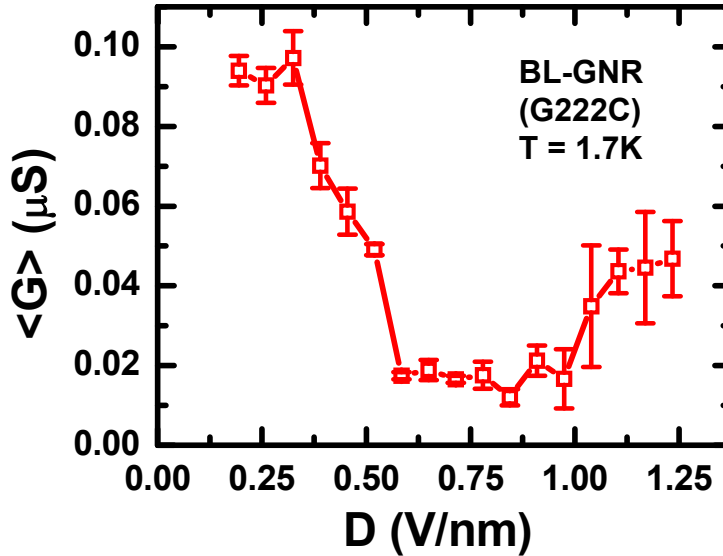
Figure 4.6 Average conductance in the transport gap versus the electric field. The average conductance values are extracted from Figure 4.4a (BL-GNR G222C).

In the case of the oscillation peaks, the averaging conductance within the gapped region ($<G_g>$) is adapted to quantify the density of the oscillations. This method has previously been used in the case of SL-GNRs to measure the number of the oscillation peaks and their average strength.[132] As shown in Figure 4.6, in BL-GNR G222C, $<G_g>$

has an inverse dependence on the D field compared to ΔE_{TR}. It remains a relatively low value (0.02 ~ 0.04 µS) in the high field regime, and increases to a higher value (~ 0.1 µS) when D reduces to below 0.6 V/nm.

The dependence of the oscillation peaks on the D field can be further illustrated by examining the individual G ~ V_{TG} curves under different D fields, as shown in Figure 4.7. At a high D field (~ 1V/nm), there is a part within the transport gap that is nearly free of oscillation peaks, except only around the edges of the transport gap (Figure 4.7c). When the D field gets lower, the oscillation peaks start to increase. At D = 0.6V/nm, multiple peaks are observed (Figure 4.7b). As the D field approaches zero (see Figure 4.7a), the peaks become denser and higher, even causing the lowest measured conductance to become higher than the high field value.
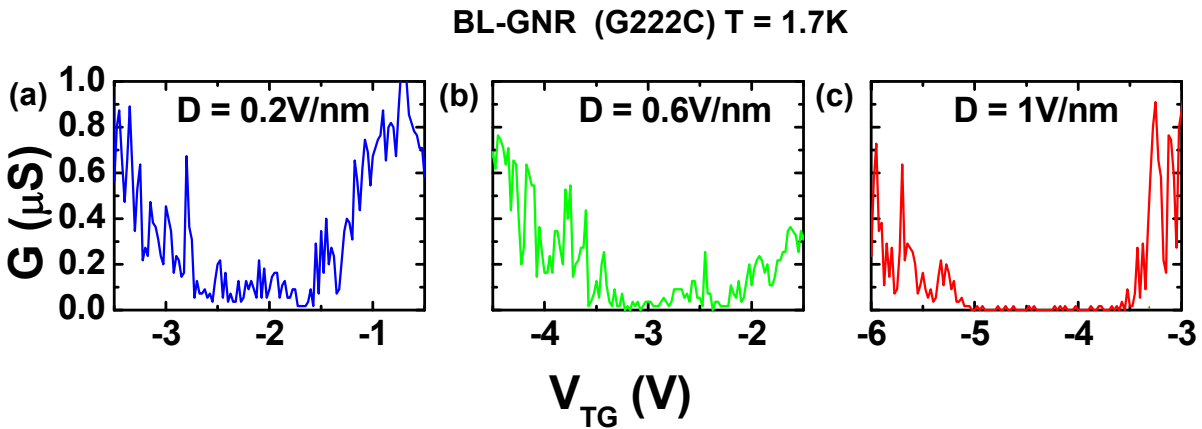
BL-GNR (G222C) T = 1.7K

Figure 4.7 Evolution of the oscillation peaks with the changing D field. Measured individual G ~V_{TG} curves from BL-GNR G222C at different perpendicular displacement field, D = 0.2V/nm, 0.6V/nm and 1V/nm. Clear differences in the oscillation peaks are observed.

It is worth noting that a direct observation like this (Figure 4.7 a, b &c) is not common in our BL-GNRs, because of the different disorder levels possessed by the BL-GNRs fabricated using current method. For the same reason, absolute values of the transport gap and average conductance vary from device to device. This can be seen from another BL-GNR sample (G246K) we fabricated using the same process, but the overall trend of ΔE_F and $<G_g>$ dependences on D/ΔE_{FD} remains the same in both devices, Figure 4.8.
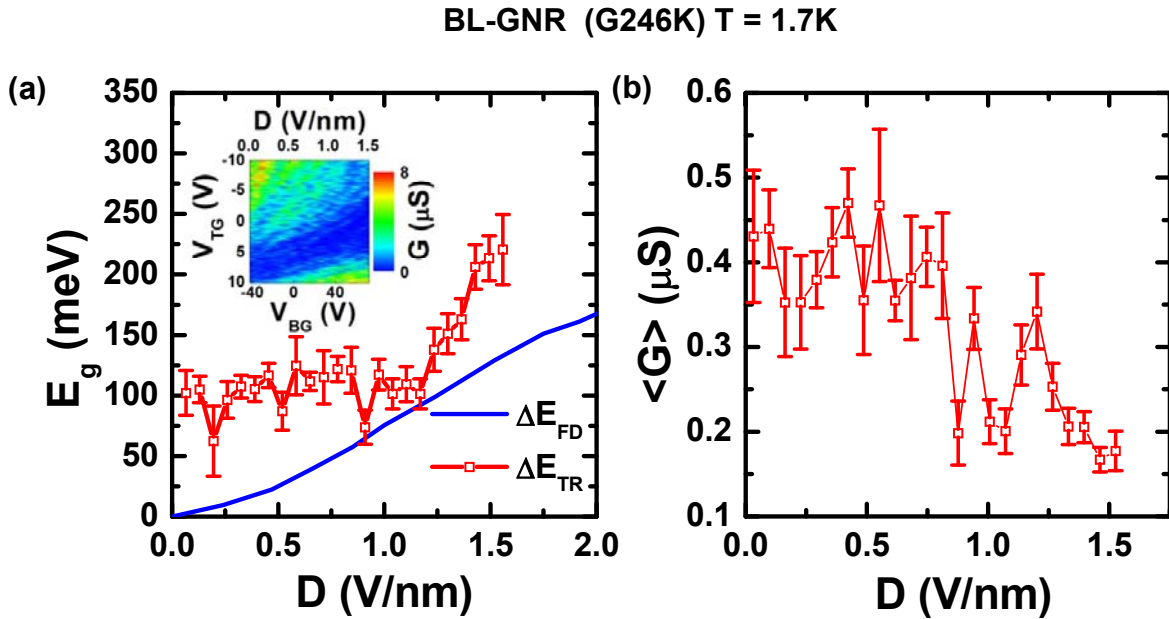
Figure 4.8 Field dependence of the Transport gap and the average conductance in BL-GNR G246K. (a) Transport gap ΔE_{TR} (red squares) and Field induced gap ΔE_{FD} (blue line) dependence on the D field. Inset: color map, $G \sim V_{TG}$ and D. (b) Averaging conductance within the transport gap, $<G_{gap}>$ versus ΔE_{FD}.

4.2.3 Interaction between the potential landscape and the field induced gap.

As we pointed out in Chapter 3, the disorders-induced potential landscape governs the transport properties in BL-GNRs, including both the transport gap and the oscillation peaks. The existence of the disorders, hence the potential landscape, remains in the dual-gated BL-GNRs, since the top-gate process does not involve any possible steps to remove them. This is also proved by the existence of the transport gap and the oscillation peaks in the $G \sim V_{TG}$ curves. At the same time, based on the analysis in this chapter, these properties are also deeply affected by the field-induced gap. Thus, we believe that the overall transport behavior in dual-gated BL-GNRs is the result of the interaction between the potential landscape and the field-induced gap.
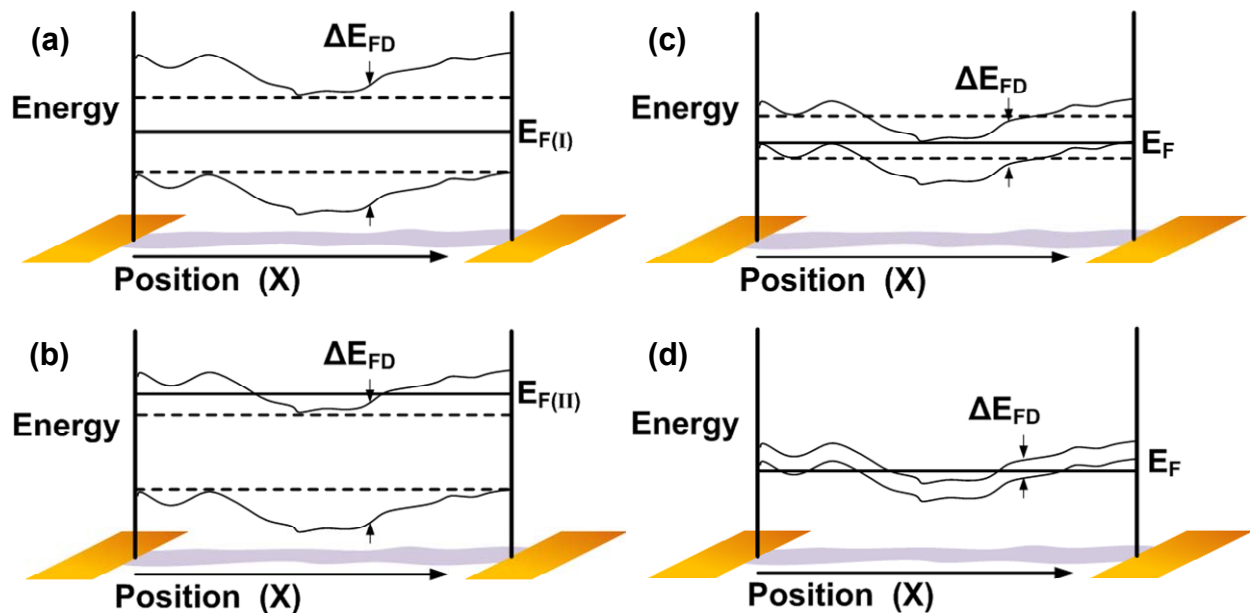
Figure 4.9 Interaction between the potential landscape and the field induced gap in BL-GNRs. (a) At a high D field with large ΔE_{FD}, when E_F in between the conduction and valence band landscapes, the 'oscillation-free' behavior can be observed. (b) When E_F crosses the potential landscape, oscillation peaks appear near the edges of the

transport gap. (c) At reduced ΔE_{FD}, the potential landscapes from conduction and valence band reach a similar level, the 'oscillation free' part disappears. (d) At a low D field with small $\Delta E_{FD,}$ the potential landscape dominates the transport. This is a resemblance to the back-gated BL-GNRs described in Chapter 3.

As a result, some modifications must be made to the model presented in Figure 3.11. The small real energy gap E_g, can be much larger in dual-gated BL-GNRs because of ΔE_{FD}, which also changes with the D fields. The potential landscape superimposed onto this energy gap forms the total band diagram of dual-gated BL-GNRs, as shown in Figure 4.9.

Based on this physical picture, changes in the transport gap size and the average conductance can be explained. At low temperatures, an insulating state appears, when the Fermi level comes cross either the real energy gap or passes through the fluctuating potential landscape. In a system with both the energy gap and the potential fluctuation, such as a BL-GNR, the dominant factor is determined by the relative strength between these two effects, which may vary under different conditions.

In the high field regime, ΔE_{FD} is large, so is the total gapped region (ΔE_{TR}). If the potential fluctuation is small enough compared to ΔE_{FD}, E_F can actually come across the real energy gap region (Figure 4.9a), giving the oscillation-free part in the G ~ V_{TG} curves, corresponding to the situation in Figure 4.7c. Oscillation peaks occur only near the edges of the transport gap, when E_F passes the potential landscape (Figure 4.9b). At this stage, the large ΔE_{FD} dominates, so the transport gap changes its size with

ΔE_{FD}, i.e., decreasing as the D field reduces. When ΔE_{FD} reaches a smaller value, the bottom of the conduction band fluctuation can be near the similar level with the top of the valence band fluctuation (Figure 4.9c). The oscillation peaks increase within the transport gap and the oscillation-free part disappears in the corresponding $G \sim V_{TG}$ curve, as shown in Figure 4.7b. As ΔE_{FD} keeps reducing, the potential landscape starts to dominate the transport (Figure 4.9d). Since the potential fluctuation is coming from the disorders, which will not be strongly affected by ΔE_{FD}, the size of the transport gap does not have large variations in this regime; neither do the density of the oscillation peaks.

It is worth mentioning that in device G222C, the fluctuation in the potential landscape is relatively small compared to the highest reachable ΔE_{FD}, which explains the small ΔE_{TR} near zero D field and the oscillation-free part in the $G \sim V_{TG}$ curve, shown in Figure 4.9a&b. This is not the case for BL-GNR G246K where only situations in Figure 4.9c&d are observed.

4.2.4 Activation energy in dual-gated BL-GNRs

Another possible way of extracting an energy gap is to monitor the temperature dependence of the conductance. In the case of an ideal defect-free insulator, thermally activated transport is expected. The conductance relates to the temperature with the following equation:

$$G \propto e^{-\frac{E_a}{kT}}$$
<div align="right">Eq.(4-5)</div>

where k is Boltzmann's constant and E_a is the activation energy, corresponding to half the band-gap.
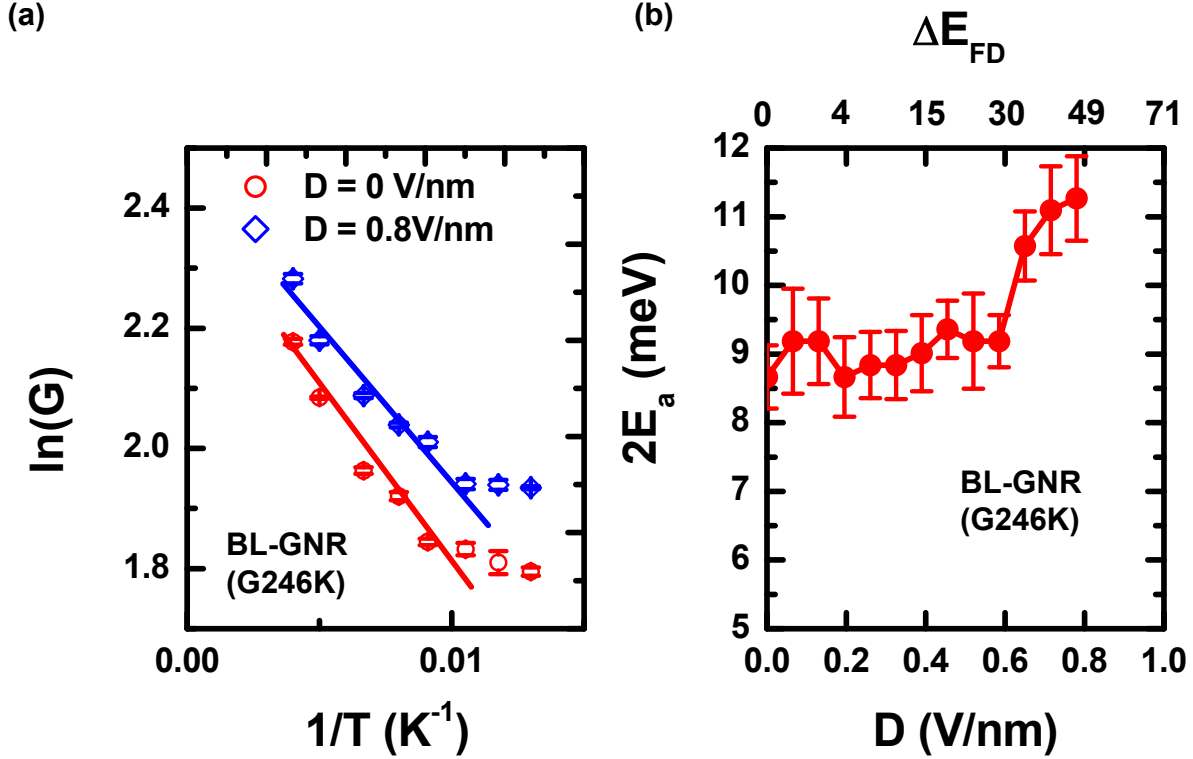
Figure 4.10 Activation energies in BL-GNRs under different D fields. (a) Linear fittings of ln(G) ~ 1/T in BL-GNR G246K. Two examples are presented for D = 0 V/nm (red dots) and D = 0.8 V/nm (blue squares) in this particular device. (b) Band-gap (2E_a) estimated from the activation energy versus the D field in this BL-GNR. The corresponding field-induced gap (ΔE_{FD}) values are listed as the top axes.

Such behaviors are indeed observed in dual-gated BL-GNRs. Between 77K to 250K, the activation energies (E_a) can be extracted from the linear fit of the lnG_{min} ~ 1/T curve at the charge neutral points (typical results shown in Figure 4.10a). However, the

energy gap obtained by this method ($2E_a$) is much smaller compared to the theoretical field-induced gap (Figure 4.10b). Similar large discrepancies have been reported in SL-GNRs, where the nearest-neighbor-hopping process is interpreted as the cause of this simple activation behavior, instead of a real energy gap.[72] Considering the disorders and the possible quantum dot states in our BL-GNRs, we believe this is also the reason for the observed E_a behavior in our experiments. Furthermore, the extracted E_a shows similar dependence on the D field as ΔE_{TR}, which corroborates the physical model we presented in Figure 4.9, indicating the hopping energy increases with ΔE_{FD} in the high D field region and remains nearly unaffected when the potential landscape dominates.
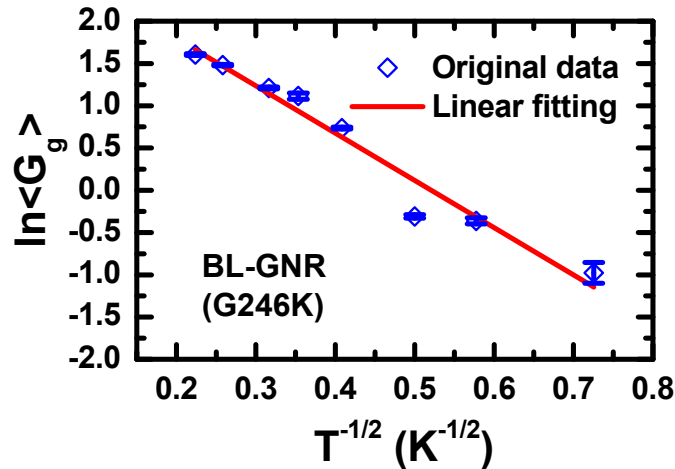
Figure 4.11 Temperature dependence of the conductance in the low T regime. Measured average conductance (in natural logarithm scale) within the transport gap at various temperatures from BL-GNR G246K. The red line is a fit to 1D variable range hopping.

It is also worth noting that in the low temperature regime, the $\ln(G) \sim 1/T$ curves deviate from the Eq. (4-5). Instead, the temperature dependence behavior follows $G \sim \exp(-(T_0/T)^{1/2})$, (see Figure 4.11a). This indicates the 1D variable range hopping (VRH) nature of the transport, which can also be explained by the disorder-induced random potential landscape. [133]

4.3 Summary

In this chapter, we studied the effects of the perpendicular electric field and the field-induced gap on the transport properties of bilayer graphene nanoribbons by fabricating and measuring dual-gated devices. The existence of the field induced gap is proved by similar behaviors compared to bilayer graphene devices at high temperatures. At low temperatures, changing of the transport gap size and the oscillation strength are uniquely observed in dual-gated BL-GNR devices. The dependences of both ΔE_{TR} and $\langle G_g \rangle$ on the electric displacement field reveal the interaction between the field-induced gap and the potential landscape at different field ranges. In the high field regime, the large field-induced gap governs the transport properties, while the potential landscape becomes the dominant factor in the low field regime.

Chapter 5

Conclusion

This thesis is motivated by the rising of the graphene electronic and the potential applications of bilayer graphene nanoribbons and focuses on understanding the basic transport properties of BL-GNRs.

In the fabrication process (Chapter 2), we use Raman spectra to select A-B stacking bilayer graphene films among the mechanical exfoliated graphene samples. Nanowire masks and the oxygen plasma etching are then used to pattern bilayer graphene nanoribbons. For dual-gated devices, we use evaporated Al thin layer, followed by the ALD grown Al_2O_3 for the top-gate dielectric.

In back-gated bilayer graphene nanoribbon devices (Chapter 3), large transport gaps appear in the transport measurements, which exceeds the size of the possible confinement gap and the field-induced gap. This indicates the important role of the disorders in the transport. Inside the transport gap, Coulomb diamonds and oscillations suggest the existence of spontaneously formed quantum dots in bilayer graphene nanoribbons. A physical picture based on the relative movement between the Fermi level and the disorder-induced potential landscape is successfully used to explain the observed transport behaviors.

For the spontaneously form quantum dots in bilayer graphene nanoribbons, the electron temperatures related to thermal fluctuations and excessive energies are both

very close to the measurement temperature, which is a clear indication of the stability of the source/drain barriers of the quantum dot. This, in turn, proves the stability of the potential landscape against the thermal fluctuation and the source/drain bias, which can be beneficial to the possible applications of bilayer graphene nanoribbons.

In the dual-gated bilayer graphene nanoribbon devices (Chapter 4), the evolution of the transport gap with the perpendicular electric field shows its distinguish signature compared to single-layer graphene nanoribbons. In the high field regime, the transport gap follows the trend of the field-induced gap with an energy difference varying from sample to sample, while remains near constant in the low field regime. This suggests the superposition of the potential landscape and the field-induced gap in bilayer graphene nanoribbons. The field dependence of the averaging conductance inside the transport gap and the extracted activation energy can also be explained based on this model. These newly observed effects not only further corroborate our previous understanding (the potential landscape picture) based on the back-gated bilayer graphene nanoribbons, but also extended the knowledge to the interaction between the field-induced gap and the existing potential landscape.

Based on our studies, in order to utilize bilayer graphene nanoribbons, the disorder-induced potential landscape needs to be either removed/reduced (by dielectric screening, suspended structures and better etching methods) or properly controlled (by fabricating local gates). And a symmetrical dual-gated structure (i.e. using thin high-κ dielectric for both gates) may be able to achieve more efficient modulation of the field-induced gap in the electrical measurements. Although many potential problems still

remain unsolved, our study from the basic transport property point of view is a good start for the future applications of bilayer graphene nanoribbons.

References

1.   Moore, G. E., Cramming more components onto integrated circuits. *Electronics Magazine* **1965,** *38* (8), 4-7.

2.   Geim, A. K.; Novoselov, K. S., The rise of graphene. *Nat. Mater.* **2007,** *6* (3), 183-191.

3.   Geim, A. K., Graphene: Status and Prospects. *Science* **2009,** *324* (5934), 1530-1534.

4.   Novoselov, K. S., Nobel Lecture: Graphene: Materials in the Flatland. *Rev. Mod. Phys.* **2011,** *83* (3), 837-849.

5.   Wright, A. R.; Cao, J. C.; Zhang, C., Enhanced Optical Conductivity of Bilayer Graphene Nanoribbons in the Terahertz Regime. *Phys. Rev. Lett.* **2009,** *103* (20), 207401.

6.   Liu, J.; Wang, B.; Ma, Z.; Zhang, C., Two-color Terahertz Response in Bilayer Graphene Nanoribbons with Spin-orbit Coupling. *Appl. Phys. Lett.* **2011,** *98* (6), 061107.

7.   Sahu, B.; Min, H.; MacDonald, A. H.; Banerjee, S. K., Energy Gaps, Magnetism, and Electric-Field Effects in Bilayer Graphene Nanoribbons. *Phys. Rev. B* **2008,** *78* (4), 045404.

8.   Kim, G.; Jhi, S.-H., Spin-polarized Energy-gap Opening in Asymmetric Bilayer Graphene Nanoribbons. *Appl. Phys. Lett.* **2010,** *97* (26), 263114.

9.   Guo, Y.; Guo, W.; Chen, C., Semiconducting to Half-Metallic to Metallic Transition on Spin-Resolved Zigzag Bilayer Graphene Nanoribbons. *J. Phys. Chem. C* **2010,** *114* (30), 13098-13105.

10.   Li, X.; Zhang, Z.; Xiao, D., Pseudospin Valve in Bilayer Graphene Nanoribbons. *Phys. Rev. B* **2010,** *81* (19), 195402.

11.   Novoselov, K. S.; Geim, A. K.; Morozov, S. V.; Jiang, D.; Katsnelson, M. I.; Grigorieva, I. V.; Dubonos, S. V.; Firsov, A. A., Two-dimensional gas of massless Dirac fermions in graphene. *Nature* **2005,** *438* (7065), 197-200.

12.   Zhang, Y.; Tan, Y.-W.; Stormer, H. L.; Kim, P., Experimental observation of the quantum Hall effect and Berry's phase in graphene. *Nature* **2005,** *438* (7065), 201-204.

13.   Wallace, P. R., The Band Theory of Graphite. *Physical Review* **1947,** *71* (9), 622.

14.   Saito, R.; Dresselhaus, G.; Dresselhaus, M. S., *Physical properties of carbon nanotubes*. World Scientific: 1998; Vol. 35.

15.   Katsnelson, M. I.; Novoselov, K. S.; Geim, A. K., Chiral Tunnelling and the Klein Paradox in Graphene. *Nat. Phys.* **2006,** *2* (9), 620-625.

16.   Young, A. F.; Kim, P., Quantum interference and Klein tunnelling in graphene heterojunctions. *Nat. Phys.* **2009,** *5* (3), 222-226.

17.   Bolotin, K. I.; Sikes, K. J.; Jiang, Z.; Klima, M.; Fudenberg, G.; Hone, J.; Kim, P.; Stormer, H. L., Ultrahigh Electron Mobility in Suspended Graphene. *Solid State Commun.* **2008,** *146* (9-10), 351-355.

18.   Bolotin, K. I.; Sikes, K. J.; Hone, J.; Stormer, H. L.; Kim, P., Temperature-Dependent Transport in Suspended Graphene. *Phys. Rev. Lett.* **2008,** *101* (9), 096802-4.

19.   Morozov, S. V.; Novoselov, K. S.; Katsnelson, M. I.; Schedin, F.; Elias, D. C.; Jaszczak, J. A.; Geim, A. K., Giant Intrinsic Carrier Mobilities in Graphene and Its Bilayer. *Phys. Rev. Lett.* **2008,** *100* (1), 016602-4.

20.   Liao, L.; Lin, Y.-C.; Bao, M.; Cheng, R.; Bai, J.; Liu, Y.; Qu, Y.; Wang, K. L.; Huang, Y.; Duan, X., High-speed graphene transistors with a self-aligned nanowire gate. *Nature* **2010,** *467* (7313), 305-308.

21.   Lin, Y.-M.; Valdes-Garcia, A.; Han, S.-J.; Farmer, D. B.; Meric, I.; Sun, Y.; Wu, Y.; Dimitrakopoulos, C.; Grill, A.; Avouris, P.; Jenkins, K. A., Wafer-Scale Graphene Integrated Circuit. *Science* **2011,** *332* (6035), 1294-1297.

22.   Lin, Y.-M.; Dimitrakopoulos, C.; Jenkins, K. A.; Farmer, D. B.; Chiu, H.-Y.; Grill, A.; Avouris, P., 100-GHz Transistors from Wafer-Scale Epitaxial Graphene. *Science* **2010,** *327* (5966), 662-.

23.   Wang, H. N., D.; Kong, J.; Palacios, T., Graphene Frequency Multipliers. *IEEE Electron Device Letters* **2009**.

24.   Wang, Z.; Zhang, Z.; Xu, H.; Ding, L.; Wang, S.; Peng, L.-M., A high-performance top-gate graphene field-effect transistor based frequency doubler. *Appl. Phys. Lett.* **2010,** *96* (17), 173104.

25.   Liu, G.; Velasco, J. J.; Bao, W.; Lau, C. N., Fabrication of graphene p-n-p junctions with contactless top gates. *Appl. Phys. Lett.* **2008,** *92* (20), 203103-3.

26.   Low, T.; Appenzeller, J., Electronic transport properties of a tilted graphene p-n junction. *Physical Review B (Condensed Matter and Materials Physics)* **2009,** *80* (15), 155406-7.

27.   Low, T.; Seokmin, H.; Appenzeller, J.; Datta, S.; Lundstrom, M. S., Conductance Asymmetry of Graphene p-n Junction. *Electron Devices, IEEE Transactions on* **2009,** *56* (6), 1292-1299.

28.   Britnell, L.; Gorbachev, R. V.; Jalil, R.; Belle, B. D.; Schedin, F.; Mishchenko, A.; Georgiou, T.; Katsnelson, M. I.; Eaves, L.; Morozov, S. V.; Peres, N. M. R.; Leist, J.;

Geim, A. K.; Novoselov, K. S.; Ponomarenko, L. A., Field-Effect Tunneling Transistor Based on Vertical Graphene Heterostructures. *Science* **2012,** *335* (6071), 947-950.

29.   Britnell, L.; Gorbachev, R. V.; Jalil, R.; Belle, B. D.; Schedin, F.; Katsnelson, M. I.; Eaves, L.; Morozov, S. V.; Mayorov, A. S.; Peres, N. M. R.; Castro Neto, A. H.; Leist, J.; Geim, A. K.; Ponomarenko, L. A.; Novoselov, K. S., Electron Tunneling through Ultrathin Boron Nitride Crystalline Barriers. *Nano Lett.* **2012**.

30.   Haigh, S. J.; Gholinia, A.; Jalil, R.; Romani, S.; Britnell, L.; Elias, D. C.; Novoselov, K. S.; Ponomarenko, L. A.; Geim, A. K.; Gorbachev, R., Cross-sectional imaging of individual layers and buried interfaces of graphene-based heterostructures and superlattices. *Nat. Mater.* **2012,** *11* (9), 764-767.

31.   Tombros, N.; Jozsa, C.; Popinciuc, M.; Jonkman, H. T.; van Wees, B. J., Electronic spin transport and spin precession in single graphene layers at room temperature. *Nature* **2007,** *448* (7153), 571-574.

32.   Han, W.; Pi, K.; Bao, W.; McCreary, K. M.; Li, Y.; Wang, W. H.; Lau, C. N.; Kawakami, R. K., Electrical detection of spin precession in single layer graphene spin valves with transparent contacts. *Appl. Phys. Lett.* **2009,** *94* (22), 222109-3.

33.   Han, W.; Wang, W. H.; Pi, K.; McCreary, K. M.; Bao, W.; Li, Y.; Miao, F.; Lau, C. N.; Kawakami, R. K., Electron-Hole Asymmetry of Spin Injection and Transport in Single-Layer Graphene. *Phys. Rev. Lett.* **2009,** *102* (13), 137205-4.

34.   Cho, S.; Chen, Y.-F.; Fuhrer, M. S., Gate-tunable graphene spin valve. *Appl. Phys. Lett.* **2007,** *91* (12), 123105.

35.   Mehr, W.; Dabrowski, J.; Scheytt, J. C.; Lippert, G.; Ya-Hong, X.; Lemme, M. C.; Ostling, M.; Lupina, G., Vertical Graphene Base Transistor. *Electron Device Letters, IEEE* **2012,** *33* (5), 691-693.

36.   Sam Vaziri; Grzegorz Lupina; Christoph Henkel; Anderson D. Smith; Mikael Östling; Jarek Dabrowski; Gunther Lippert; Wolfgang Mehr; Lemme, M. C., A Graphene-based Hot Electron Transistor. *arXiv:1211.2949v1 [cond-mat.mes-hall]* **2012**.

37.   B. D. Kong; C. Zeng; D. K. Gaskill; K. L. Wang; Kim, K. W., Two Dimensional Crystal Tunneling Devices for THz Operation. *arXiv:1211.1593v1 [cond-mat.mtrl-sci]* **2012**.

38.   Mak, K. F.; Shan, J.; Heinz, T. F., Electronic Structure of Few-Layer Graphene: Experimental Demonstration of Strong Dependence on Stacking Sequence. *Phys. Rev. Lett.* **2010,** *104* (17), 176404.

39.   Bernal, J. D., The Structure of Graphite. *Proceedings of the Royal Society of London. Series A* **1924,** *106* (740), 749-773.

40.   Neto, A. H. C.; Guinea, F.; Peres, N. M. R.; Novoselov, K. S.; Geim, A. K., The Electronic Properties of Graphene. *Rev. Mod. Phys.* **2009,** *81* (1), 109-54.

41.   McCann, E.; Abergel, D. S. L.; Fal'ko, V. I., Electrons in Bilayer Graphene. *Solid State Commun.* **2007,** *143* (1-2), 110-115.

42.   Singh, J., *Electronic and optoelectronic properties of semiconductor structures*. Cambridge University Press: 2003.

43.   Min, H.; Sahu, B.; Banerjee, S. K.; MacDonald, A. H., Ab Initio Theory of Gate Induced Gaps in Graphene Bilayers. *Phys. Rev. B* **2007,** *75* (15), 155115-7.

44.   Ohta, T.; Bostwick, A.; Seyller, T.; Horn, K.; Rotenberg, E., Controlling the Electronic Structure of Bilayer Graphene. *Science* **2006,** *313* (5789), 951-954.

45.   Castro, E. V.; Novoselov, K. S.; Morozov, S. V.; Peres, N. M. R.; dos Santos, J. M. B. L.; Nilsson, J.; Guinea, F.; Geim, A. K.; Neto, A. H. C., Biased Bilayer Graphene: Semiconductor with a Gap Tunable by the Electric Field Effect. *Phys. Rev. Lett.* **2007,** *99* (21), 216802.

46.   Oostinga, J. B.; Heersche, H. B.; Liu, X.; Morpurgo, A. F.; Vandersypen, L. M. K., Gate-Induced Insulating State in Bilayer Graphene Devices. *Nat. Mater.* **2008,** *7* (2), 151-157.

47.   Kuzmenko, A. B.; Crassee, I.; van der Marel, D.; Blake, P.; Novoselov, K. S., Determination of the gate-tunable band gap and tight-binding parameters in bilayer graphene using infrared spectroscopy. *Phys. Rev. B* **2009,** *80* (16), 165406.

48.   Kuzmenko, A. B.; van Heumen, E.; van der Marel, D.; Lerch, P.; Blake, P.; Novoselov, K. S.; Geim, A. K., Infrared spectroscopy of electronic bands in bilayer graphene. *Phys. Rev. B* **2009,** *79* (11), 115441.

49.   Zhang, Y.; Tang, T.-T.; Girit, C.; Hao, Z.; Martin, M. C.; Zettl, A.; Crommie, M. F.; Shen, Y. R.; Wang, F., Direct Observation of a Widely Tunable Bandgap in Bilayer Graphene. *Nature* **2009,** *459* (7248), 820-823.

50.   Eduardo, V. C.; Novoselov, K. S.; Morozov, S. V.; Peres, N. M. R.; Santos, J. M. B. L. d.; Johan, N.; Guinea, F.; Geim, A. K.; Neto, A. H. C., Electronic properties of a biased graphene bilayer. *Journal of Physics: Condensed Matter* **2010,** *22* (17), 175503.

51.   Xia, F.; Farmer, D. B.; Lin, Y.-m.; Avouris, P., Graphene Field-Effect Transistors with High On/Off Current Ratio and Large Transport Band Gap at Room Temperature. *Nano Lett.* **2010,** *10* (2), 715-718.

52.   Chen, Z.; Lin, Y.-M.; Rooks, M. J.; Avouris, P., Graphene nano-ribbon electronics. *Physica E: Low-dimensional Systems and Nanostructures* **2007,** *40* (2), 228-232.

53.   Han, M. Y.; Ozyilmaz, B.; Zhang, Y.; Kim, P., Energy Band-Gap Engineering of Graphene Nanoribbons. *Phys. Rev. Lett.* **2007,** *98* (20), 206805-4.

54.   Ezawa, M., Peculiar width dependence of the electronic properties of carbon nanoribbons. *Phys. Rev. B* **2006,** *73* (4), 045432.

55.   Peres, N. M. R.; Castro Neto, A. H.; Guinea, F., Conductance quantization in mesoscopic graphene. *Phys. Rev. B* **2006,** *73* (19), 195411.

56.   Brey, L.; Fertig, H. A., Electronic states of graphene nanoribbons studied with the Dirac equation. *Phys. Rev. B* **2006,** *73* (23), 235411.

57.   Son, Y.-W.; Cohen, M. L.; Louie, S. G., Energy Gaps in Graphene Nanoribbons. *Phys. Rev. Lett.* **2006,** *97* (21), 216803.

58.   Martin, J.; Akerman, N.; Ulbricht, G.; Lohmann, T.; Smet, J. H.; von Klitzing, K.; Yacoby, A., Observation of Electron-hole Puddles in Graphene Using a Scanning Single-electron Transistor. *Nat. Phys.* **2008,** *4* (2), 144-148.

59.   Jia, X.; Hofmann, M.; Meunier, V.; Sumpter, B. G.; Campos-Delgado, J.; Romo-Herrera, J. M.; Son, H.; Hsieh, Y.-P.; Reina, A.; Kong, J.; Terrones, M.; Dresselhaus, M. S., Controlled Formation of Sharp Zigzag and Armchair Edges in Graphitic Nanoribbons. *Science* **2009,** *323* (5922), 1701-1705.

60.   Kobayashi, Y.; Fukui, K.-i.; Enoki, T.; Kusakabe, K.; Kaburagi, Y., Observation of zigzag and armchair edges of graphite using scanning tunneling microscopy and spectroscopy. *Phys. Rev. B* **2005,** *71* (19), 193406.

61.   Koskinen, P.; Malola, S.; Häkkinen, H., Evidence for graphene edges beyond zigzag and armchair. *Phys. Rev. B* **2009,** *80* (7), 073401.

62.   Sols, F.; Guinea, F.; Neto, A. H. C., Coulomb Blockade in Graphene Nanoribbons. *Phys. Rev. Lett.* **2007,** *99* (16), 166803.

63.   Mucciolo, E. R.; Castro Neto, A. H.; Lewenkopf, C. H., Conductance Quantization and Transport Gaps in Disordered Graphene Nanoribbons. *Phys. Rev. B* **2009,** *79* (7), 075407.

64.   Evaldsson, M.; Zozoulenko, I. V.; Xu, H.; Heinzel, T., Edge-disorder-induced Anderson Localization and Conduction Gap in Graphene Nanoribbons. *Phys. Rev. B* **2008,** *78* (16), 161407.

65.   Ponomarenko, L. A.; Schedin, F.; Katsnelson, M. I.; Yang, R.; Hill, E. W.; Novoselov, K. S.; Geim, A. K., Chaotic Dirac Billiard in Graphene Quantum Dots. *Science* **2008,** *320* (5874), 356-358.

66.   Stampfer, C.; Guttinger, J.; Hellmuller, S.; Molitor, F.; Ensslin, K.; Ihn, T., Energy Gaps in Etched Graphene Nanoribbons. *Phys. Rev. Lett.* **2009,** *102* (5), 056403.

67.   Todd, K.; Chou, H.-T.; Amasha, S.; Goldhaber-Gordon, D., Quantum Dot Behavior in Graphene Nanoconstrictions. *Nano Lett.* **2009,** *9* (1), 416-421.

68.   Liu, X.; Oostinga, J. B.; Morpurgo, A. F.; Vandersypen, L. M. K., Electrostatic confinement of electrons in graphene nanoribbons. *Phys. Rev. B* **2009,** *80* (12), 121407.

69.   Gallagher, P.; Todd, K.; Goldhaber-Gordon, D., Disorder-induced Gap Behavior in Graphene Nanoribbons. *Phys. Rev. B* **2010,** *81* (11), 115409.

70.   Molitor, F.; Jacobsen, A.; Stampfer, C.; uuml; ttinger, J.; Ihn, T.; Ensslin, K., Transport Gap in Side-gated Graphene Constrictions. *Phys. Rev. B* **2009,** *79* (7), 075426.

71.   Molitor, F.; Stampfer, C.; Guttinger, J.; Jacobsen, A.; Ihn, T.; Ensslin, K., Energy and Transport Gaps in Etched Graphene Nanoribbons. *Semicond. Sci. Technol.* **2010,** *25* (3), 034002.

72.   Han, M. Y.; Brant, J. C.; Kim, P., Electron Transport in Disordered Graphene Nanoribbons. *Phys. Rev. Lett.* **2010,** *104* (5), 056801.

73.   Xu, G.; Torres, C. M.; Song, E. B.; Tang, J.; Bai, J.; Duan, X.; Zhang, Y.; Wang, K. L., Enhanced Conductance Fluctuation by Quantum Confinement Effect in Graphene Nanoribbons. *Nano Lett.* **2010,** *10* (11), 4590-4594.

74.   Wang, X.; Ouyang, Y.; Li, X.; Wang, H.; Guo, J.; Dai, H., Room-Temperature All-Semiconducting Sub-10-nm Graphene Nanoribbon Field-Effect Transistors. *Phys. Rev. Lett.* **2008,** *100* (20), 206803.

75.   Purewal, M. S.; Hong, B. H.; Ravi, A.; Chandra, B.; Hone, J.; Kim, P., Scaling of Resistance and Electron Mean Free Path of Single-Walled Carbon Nanotubes. *Phys. Rev. Lett.* **2007,** *98* (18), 186808.

76.   Son, Y.-W.; Cohen, M. L.; Louie, S. G., Half-metallic graphene nanoribbons. *Nature* **2006,** *444* (7117), 347-349.

77.   Lam, K.-T.; Liang, G., An ab initio study on energy gap of bilayer graphene nanoribbons with armchair edges. *Appl. Phys. Lett.* **2008,** *92* (22), 223106.

78.   Sahu, B.; Min, H.; Banerjee, S. K., Effects of edge magnetism and external electric field on energy gaps in multilayer graphene nanoribbons. *Phys. Rev. B* **2010,** *82* (11), 115426.

79.   Szafranek, B. N.; Schall, D.; Otto, M.; Neumaier, D.; Kurz, H., Electrical observation of a tunable band gap in bilayer graphene nanoribbons at room temperature. *Appl. Phys. Lett.* **2010,** *96* (11), 112103.

80.   Xu, G.; Bai, J.; Carlos M. Torres, J.; Song, E. B.; Tang, J.; Zhou, Y.; Duan, X.; Zhang, Y.; Wang, K. L., Low-noise submicron channel graphene nanoribbons. *Appl. Phys. Lett.* **2010,** *97* (7), 073107.

81.   Xu, G.; Torres, C. M.; Zhang, Y.; Liu, F.; Song, E. B.; Wang, M.; Zhou, Y.; Zeng, C.; Wang, K. L., Effect of Spatial Charge Inhomogeneity on 1/f Noise Behavior in Graphene. *Nano Lett.* **2010,** *10* (9), 3312-3317.

82.   Bai, J.; Duan, X.; Huang, Y., Rational Fabrication of Graphene Nanoribbons Using a Nanowire Etch Mask. *Nano Lett.* **2009,** *9* (5), 2083-2087.

83.   Kosynkin, D. V.; Higginbotham, A. L.; Sinitskii, A.; Lomeda, J. R.; Dimiev, A.; Price, B. K.; Tour, J. M., Longitudinal Unzipping of Carbon Nanotubes to Form Graphene Nanoribbons. *Nature* **2009,** *458* (7240), 872-876.

84.   Li, X.; Wang, X.; Zhang, L.; Lee, S.; Dai, H., Chemically Derived, Ultrasmooth Graphene Nanoribbon Semiconductors. *Science* **2008,** *319* (5867), 1229-1232.

85.   Novoselov, K. S.; Geim, A. K.; Morozov, S. V.; Jiang, D.; Zhang, Y.; Dubonos, S. V.; Grigorieva, I. V.; Firsov, A. A., Electric Field Effect in Atomically Thin Carbon Films. *Science* **2004,** *306* (5696), 666-669.

86.   Dresselhaus, M. S.; Dresselhaus, G., Intercalation compounds of graphite. *Advances in Physics* **2002,** *51* (1), 1 - 186.

87.   Moser, J.; Barreiro, A.; Bachtold, A., Current-induced cleaning of graphene. *Appl. Phys. Lett.* **2007,** *91* (16), 163513-3.

88.   Li, X.; Cai, W.; An, J.; Kim, S.; Nah, J.; Yang, D.; Piner, R.; Velamakanni, A.; Jung, I.; Tutuc, E.; Banerjee, S. K.; Colombo, L.; Ruoff, R. S., Large-Area Synthesis of High-Quality and Uniform Graphene Films on Copper Foils. *Science* **2009,** *324* (5932), 1312-1314.

89.   Reina, A.; Jia, X.; Ho, J.; Nezich, D.; Son, H.; Bulovic, V.; Dresselhaus, M. S.; Kong, J., Large Area, Few-Layer Graphene Films on Arbitrary Substrates by Chemical Vapor Deposition. *Nano Lett.* **2008,** *9* (1), 30-35.

90.   Kim, K. S.; Zhao, Y.; Jang, H.; Lee, S. Y.; Kim, J. M.; Kim, K. S.; Ahn, J.-H.; Kim, P.; Choi, J.-Y.; Hong, B. H., Large-scale pattern growth of graphene films for stretchable transparent electrodes. *Nature* **2009,** *457* (7230), 706-710.

91.   Bae, S.; Kim, H.; Lee, Y.; Xu, X.; Park, J.-S.; Zheng, Y.; Balakrishnan, J.; Lei, T.; Ri Kim, H.; Song, Y. I.; Kim, Y.-J.; Kim, K. S.; Ozyilmaz, B.; Ahn, J.-H.; Hong, B. H.; Iijima, S., Roll-to-roll production of 30-inch graphene films for transparent electrodes. *Nat Nano* **2010,** *5* (8), 574-578.

92.   Wu, Y.; Chou, H.; Ji, H.; Wu, Q.; Chen, S.; Jiang, W.; Hao, Y.; Kang, J.; Ren, Y.; Piner, R. D.; Ruoff, R. S., Growth Mechanism and Controlled Synthesis of AB-Stacked Bilayer Graphene on Cu - Ni Alloy Foils. *ACS Nano* **2012,** *6* (9), 7731-7738.

93.   Rasool, H. I.; Song, E. B.; Allen, M. J.; Wassei, J. K.; Kaner, R. B.; Wang, K. L.; Weiller, B. H.; Gimzewski, J. K., Continuity of Graphene on Polycrystalline Copper. *Nano Lett.* **2011,** *11* (1), 251-256.

94.   Berger, C.; Song, Z.; Li, T.; Li, X.; Ogbazghi, A. Y.; Feng, R.; Dai, Z.; Marchenkov, A. N.; Conrad, E. H.; First, P. N.; de Heer, W. A., Ultrathin Epitaxial Graphite: 2D Electron Gas Properties and a Route toward Graphene-based Nanoelectronics. *The Journal of Physical Chemistry B* **2004,** *108* (52), 19912-19916.

95.   Yuehua, X.; Xiaowei, L.; Jinming, D., Infrared and Raman spectra of AA-stacking bilayer graphene. *Nanotechnology* **2010,** *21* (6), 065711.

96.   Anders, H., *Thin films in optics*. Focal P.: 1967.

97.   Song, E. B.; Lian, B.; Xu, G.; Yuan, B.; Zeng, C.; Chen, A.; Wang, M.; Kim, S.; Lang, M.; Zhou, Y.; Wang, K. L., Visibility and Raman spectroscopy of mono and bilayer graphene on crystalline silicon. *Appl. Phys. Lett.* **2010,** *96* (8), 081911.

98.   Song, E. B.; Lian, B.; Kim, S. M.; Lee, S.; Chung, T.-K.; Wang, M.; Zeng, C.; Xu, G.; Wong, K.; Zhou, Y.; Rasool, H. I.; Seo, D. H.; Chung, H.-J.; Heo, J.; Seo, S.; Wang, K. L., Robust bi-stable memory operation in single-layer graphene ferroelectric memory. *Appl. Phys. Lett.* **2011,** *99* (4), 042109.

99.   Ferrari, A. C., Raman spectroscopy of graphene and graphite: Disorder, electron-phonon coupling, doping and nonadiabatic effects. *Solid State Commun.* **2007,** *143* (1-2), 47-57.

100.   Reich, S.; Thomsen, C., Raman spectroscopy of graphite. *Philosophical Transactions of the Royal Society of London. Series A: Mathematical, Physical and Engineering Sciences* **2004,** *362* (1824), 2271-2288.

101.   Ferrari, A. C.; Meyer, J. C.; Scardaci, V.; Casiraghi, C.; Lazzeri, M.; Mauri, F.; Piscanec, S.; Jiang, D.; Novoselov, K. S.; Roth, S.; Geim, A. K., Raman Spectrum of Graphene and Graphene Layers. *Phys. Rev. Lett.* **2006,** *97* (18), 187401-4.

102.   Malard, L. M.; Pimenta, M. A.; Dresselhaus, G.; Dresselhaus, M. S., Raman spectroscopy in graphene. *Physics Reports* **2009,** *473* (5-6), 51-87.

103.   Novoselov, K. S.; McCann, E.; Morozov, S. V.; Fal'ko, V. I.; Katsnelson, M. I.; Zeitler, U.; Jiang, D.; Schedin, F.; Geim, A. K., Unconventional quantum Hall effect and Berry/'s phase of 2[pi] in bilayer graphene. *Nat. Phys.* **2006,** *2* (3), 177-180.

104.   Jung, Y. S.; Ross, C. A., Well-Ordered Thin-Film Nanopore Arrays Formed Using a Block-Copolymer Template. *Small* **2009,** *5* (14), 1654-1659.

105.   Zeng, C.; Wang, M.; Zhou, Y.; Lang, M.; Lian, B.; Song, E.; Xu, G.; Tang, J.; Torres, C.; Wang, K. L., Tunneling spectroscopy of metal-oxide-graphene structure. *Appl. Phys. Lett.* **2010,** *97* (3), 032104.

106.   Kim, S.; Nah, J.; Jo, I.; Shahrjerdi, D.; Colombo, L.; Yao, Z.; Tutuc, E.; Banerjee, S. K., Realization of a High Mobility Dual-Gated Graphene Field-Effect Transistor with Al[sub 2]O[sub 3] Dielectric. *Appl. Phys. Lett.* **2009,** *94* (6), 062107-3.

107.   Lin, Y.-M.; Perebeinos, V.; Chen, Z.; Avouris, P., Electrical Observation of Subband Formation in Graphene Nanoribbons. *Phys. Rev. B* **2008,** *78* (16), 161409.

108.   Shylau, A. A.; Klstrokos, J. W.; Zozoulenko, I. V., Capacitance of Graphene Nanoribbons. *Phys. Rev. B* **2009,** *80* (20), 205402.

109.   Deshpande, A.; Bao, W.; Zhao, Z.; Lau, C. N.; LeRoy, B. J., Mapping the Dirac Point in Gated Bilayer Graphene. *Appl. Phys. Lett.* **2009,** *95* (24), 243502.

110.   Zhang, Y.; Brar, V. W.; Girit, C.; Zettl, A.; Crommie, M. F., Origin of spatial charge inhomogeneity in graphene. *Nat. Phys.* **2009,** *advance online publication*.

111.   Xu, H.; Heinzel, T.; Zozoulenko, I. V., Edge disorder and localization regimes in bilayer graphene nanoribbons. *Phys. Rev. B* **2009,** *80* (4), 045308.

112.   Lee Eduardo, J. H.; Balasubramanian, K.; Weitz, R. T.; Burghard, M.; Kern, K., Contact and edge effects in graphene devices. *Nat Nano* **2008,** *3* (8), 486-490.

113.   Xu, G.; Torres, J. C. M.; Bai, J.; Tang, J.; Yu, T.; Huang, Y.; Duan, X.; Zhang, Y.; Wang, K. L., Linewidth Roughness in Nanowire-mask-based Graphene Nanoribbons. *Appl. Phys. Lett.* **2011,** *98*, 243118.

114.   Kouwenhoven, L. P.; Marcus, C. M.; McEuen, P. L.; Tarucha, S.; Westervelt, R. M.; Wingreen, N. S. In *Electron Transport in Quantum Dots*, Proceedings of the NATO Advanced Study Institute on Mesoscopic Electron Transport, Sohn, L. L.; Kouwenhoven, L. P.; Schon, G., Eds. Kluwer Academic Publishers: 1997; pp 105-214.

115.   Volk, C.; Fringes, S.; Terreés, B.; Dauber, J.; Engels, S.; Trellenkamp, S.; Stampfer, C., Electronic Excited States in Bilayer Graphene Double Quantum Dots. *Nano Lett.* **2011,** *11* (9), 3581-3586.

116.   Fringes, S.; Volk, C.; Norda, C.; Terrés, B.; Dauber, J.; Engels, S.; Trellenkamp, S.; Stampfer, C., Charge detection in a bilayer graphene quantum dot. *physica status solidi (b)* **2011,** *248* (11), 2684-2687.

117.   Ruzin, I. M.; Chandrasekhar, V.; Levin, E. I.; Glazman, L. I., Stochastic Coulomb Blockade in a Double-dot System. *Phys. Rev. B* **1992,** *45* (23), 13469.

118.   Ishikuro, H.; Hiramoto, T., Quantum Mechanical Effects in the Silicon Quantum Dot in a Single-electron Transistor. *Appl. Phys. Lett.* **1997,** *71* (25), 3691-3693.

119.   Ishikuro, H.; Fujii, T.; Saraya, T.; Hashiguchi, G.; Hiramoto, T.; Ikoma, T., Coulomb Blockade Oscillations at Room Temperature in a Si Quantum Wire Metal-oxide-semiconductor Field-effect Transistor Fabricated by Anisotropic Etching on a Silicon-on-insulator Substrate. *Appl. Phys. Lett.* **1996,** *68* (25), 3585-3587.

120.   Lee, S.; Hiramoto, T., Strong Dependence of Tunneling Transport Properties on Overdriving Voltage for Room-temperature-operating Single Electron/Hole Transistors Formed with Ultranarrow [100] Silicon Nanowire Channel. *Appl. Phys. Lett.* **2008,** *93* (4), 043508.

121.   Takahashi, Y.; Horiguchi, S.; Fujiwara, A.; Murase, K., Co-tunneling Current in Very Small Si Single-electron Transistors. *Phys. B* **1996,** *227* (1-4), 105-108.

122.   De Franceschi, S.; Sasaki, S.; Elzerman, J. M.; van der Wiel, W. G.; Tarucha, S.; Kouwenhoven, L. P., Electron Cotunneling in a Semiconductor Quantum Dot. *Phys. Rev. Lett.* **2001,** *86* (5), 878.

123.   Das Sarma, S.; Hwang, E. H.; Rossi, E., Theory of Carrier Transport in Bilayer Graphene. *Phys. Rev. B* **2010,** *81* (16), 161407.

124.   Hwang, E. H.; Das Sarma, S., Insulating Behavior in Metallic Bilayer Graphene: Interplay Between Density Inhomogeneity and Temperature. *Phys. Rev. B* **2010,** *82* (8), 081409.

125.   Adam, S.; Hwang, E. H.; Galitski, V. M.; Das Sarma, S., A Self-consistent Theory for Graphene Transport. *Proc. Natl. Acad. Sci.* **2007,** *104* (47), 18392-18397.

126.   Chen, F.; Xia, J.; Ferry, D. K.; Tao, N., Dielectric Screening Enhanced Performance in Graphene FET. *Nano Lett.* **2009,** *9* (7), 2571-2574.

127.   Wang, X.; Dai, H., Etching and narrowing of graphene from the edges. *Nat Chem* **2010,** *2* (8), 661-665.

128.   Jiao, L.; Zhang, L.; Wang, X.; Diankov, G.; Dai, H., Narrow Graphene Nanoribbons from Carbon Nanotubes. *Nature* **2009,** *458* (7240), 877-880.

129.   Datta, S. S.; Strachan, D. R.; Khamis, S. M.; Johnson, A. T. C., Crystallographic Etching of Few-Layer Graphene. *Nano Lett.* **2008,** *8* (7), 1912-1915.

130.   Yang, R.; Zhang, L.; Wang, Y.; Shi, Z.; Shi, D.; Gao, H.; Wang, E.; Zhang, G., An Anisotropic Etching Effect in the Graphene Basal Plane. *Advanced Materials* **2010,** *22* (36), 4014-4019.

131.   Sze, S. M.; Ng, K. K., *Physics of Semiconductor Devices*. Wiley: 2006.

132.   Oostinga, J. B.; Sac; eacute; Benjamin; Craciun, M. F.; Morpurgo, A. F., Magnetotransport through graphene nanoribbons. *Phys. Rev. B* **2010,** *81* (19), 193408.

133.   Nazarov, Y. V.; Blanter, Y. M., *Quantum Transport: Introduction to Nanoscience*. Cambridge University Press: 2009.